Simulations of Zeeman-split Ca II K-line Stokes profiles with angle-dependent partial redistribution

J.H.M.J. Bruls[1,2] **and S.K. Solanki**[3]

[1] Kiepenheuer-Institut für Sonnenphysik, Schöneckstr. 6, D-79104 Freiburg, Germany
[2] Instituto de Astrofísica de Canarias, C./ Via Láctea s/n, E-38200 La Laguna, Tenerife, Spain
[3] Institut für Astronomie, ETH–Zentrum, CH-8092 Zürich, Switzerland

Abstract. The formulation of the polarized radiative transfer equations for Zeeman-split spectral lines is still incomplete for cases with frequency-dependent line source function, e.g. when partial frequency distribution (PRD) of line photons occurs (strong resonance lines). Under the well-founded assumption that the field-free approximation works equally well for lines with partial redistribution as for lines with complete redistribution (CRD), we decouple the computation of the level populations (accounting for PRD effects) from the formal Stokes vector solution. The level populations are obtained with the Hubený & Lites (1995) version of Carlsson's (1986) MULTI code, and the formal solution follows by means of a modified version of the Murphy & Rees (1990) SPSR code. Due to lack of the appropriate equations concerning the combination of partial redistribution and Zeeman splitting of spectral lines, an ad hoc partial redistribution approach (basically allowing for wavelength dependence of the line source function) is implemented in the SPSR code. This combination of codes is used to study the relevance of partial redistribution to the Ca II K-line diagnostics of solar plage regions using grids of flux-tube models.

In addition to magnetic fields, velocity fields play an important role in the formation of the K-line profiles, but these invalidate the commonly-used angle-averaged PRD formalism. We therefore extended the Hubený & Lites (1995) angle-averaged PRD version of MULTI code to the angle-dependent case, which allows line profiles to be computed under PRD conditions for arbitrary (but not too large) velocity fields. This code is subsequently used to perform the non-magnetic non-LTE statistical equilibrium computations for a few schematic velocity structures in plage flux tubes and in the surrounding non-magnetic atmosphere. The SPSR code is again used to obtain the K-line Stokes profiles. We investigate in particular the asymmetry of the K line intensity and circularly polarized profiles produced by the velocity fields.

1. Introduction

The Ca II H & K resonance lines provide a wealth of diagnostic indicators for solar and cool-star chromospheric activity studies (Linsky & Avrett 1970; Schrijver 1995). Their high formation in the atmosphere contributes to their diagnostic value, but it also poses specific radiative transfer problems when analysing the data. Most notably, in the chromosphere the assumption of complete frequency redistribution (CRD) of line photons is no longer valid and partial redistribution (PRD) has to be invoked to explain the details of the emergent line profiles and their center-to-limb variation.

The theoretical description of partial redistribution has been developed (Hummer 1962; Oxenius 1965; Omont et al. 1972; Heinzel 1981; Hubený 1981, 1982, 1985b; Hubený et al. 1983a,b; Hubený & Cooper 1986) and efficient computational methods (Cannon et al. 1975; Vardavas & Cannon 1976; Scharmer 1983; Hubený 1985b; Uitenbroek 1989; Auer & Paletou 1994; Paletou & Auer 1995; Hubený & Lites 1995) are now available to solve the multi-level non-LTE radiative transfer problem including partial redistribution.

Presently available PRD codes assume angle-averaged partial redistribution of the line photons, which has been shown to be sufficiently accurate for static atmospheres, but to fail for dynamic ones (Hummer 1968; Milkey et al. 1975). In dynamic atmospheres line profiles that actually need to be computed with partial redistribution have been computed with CRD (e.g., Carlsson & Stein 1992). This has been a much safer choice than angle-averaged PRD, which when used in moving atmospheres produces erroneous results (e.g. Cannon & Vardavas 1974; Magnan 1974; Mihalas et al. 1976). However, when the amount of radiative energy losses needs to be computed, CRD

may not be a suitable option. Therefore Hünerth & Ulmschneider (1995) computed Mg II k-line profiles for atmospheres with shocks with a angle-dependent PRD code (Ulmschneider 1994), but using only one angle-quadrature point. Essentially that reduces the complexity of the scattering matrix and the computational effort to the level of an angle-averaged PRD computation.

In order to solve the radiative transfer problem with partial frequency redistribution in atmospheres with mass flows we either need to transform the problem to the co-moving frame, which allows application of angle-averaged PRD (Mihalas et al. 1976), or take into account the complete angle-dependence of the scattering problem in the observer's frame. The co-moving-frame method provides most gain in case of high flow speeds, but is not particularly suited for dealing with non-monotonic flow fields (Mihalas 1980a,b; see Nagendra 1996 for an application to polarized line profiles). The observer's frame method, on the other hand, requires large numbers of angle-frequency points to cope with high speed flow fields, but places no restrictions on the depth variation of the velocities. For modeling the Ca II K line in solar plage flux tubes, which contain only moderate velocities that may be non-monotonic, the observer's frame method is the appropriate choice. In Sect. 2 we therefore extend the angle-averaged PRD formulation of Hubený & Lites (1995) to the angle-dependent case.

Recently, observations of the Ca II H & K lines with circular polarization information have been obtained (Martínez Pillet et al. 1990; del Toro Iniesta et al. 1991; Trujillo-Bueno et al. 1993). Considering the distinct and significant differences that PRD has on the profiles of the H and K lines, already in the absence of magnetic fields, especially on the shape and size of the diagnostically very important H_2 and K_2 emission peaks, it is worth trying to quantify these PRD effects also in the presence of magnetic fields and for the complete Stokes vector $\boldsymbol{I} = (I, Q, U, V)^{\mathrm{T}}$.

However, the analysis of such data is far from trivial, because Zeeman splitting and partial redistribution together produce complicated line profiles. Their analysis in principle requires consistent joint solution of the Stokes vector transfer equations and the statistical equilibrium equations with the correct line photon scattering mechanism included. Efforts towards a theoretical formulation of such problems have been undertaken (e.g., Omont et al. 1973, Streater et al. 1988), but so far the theory only covers specifically limited cases.

For example, Rees & Saliba (1982) studied the influence of the line photon scattering formalism on resonance line polarization in the absence of magnetic fields. For that case the pertinent equations are well known. For the strongly related case of the Hanle effect, mainly employed to measure weak magnetic fields at the solar limb, equations have been derived for a CRD line source function (Landi Degl'Innocenti 1985), but a rigorous formalism for a PRD line source function is still lacking. An approximate expression for the line source function vector of PRD lines has been derived by Omont et al. (1973) and incorporated in a numerical method for investigating the Hanle effect by Faurobert-Scholl (1991, 1992, 1994). The general case of PRD combined with Zeeman splitting has not been solved yet, but

see Landi Degl'Innocenti et al. (1997) for promising progress in the development of the theory.

In this paper we attempt to quantify the effect of PRD on the Zeeman-split Ca II K Stokes vectors in an ad hoc fashion, where the field-free approximation is invoked to decouple the effects of the magnetic field from the statistical equilibrium computations. First the non-LTE scalar radiative transfer equations and the statistical equilibrium are solved taking into account (angle-dependent) PRD effects on the photon scattering. Afterwards the resulting line opacities and wavelength-dependent PRD line source functions are used to solve for the emergent Stokes vector for a given magnetic field configuration by means of the Stokes Profile Synthesis Routines (SPSR) of Murphy & Rees (1990), based on the diagonal element lambda operator (DELO) method (Rees et al. 1989, henceforth RMD).

The field-free approach, used in the first step of this procedure, has been shown by Rees (1969), Auer et al. (1977) and Bruls & Trujillo Bueno (1996) to be a good approximation for the Ca II H & K lines, be it under the additional assumption of complete frequency redistribution. Considering that the core parts of a line contribute most in setting the statistical equilibrium and that complete redistribution is perfectly valid for the H and K-line cores, the influence of a magnetic field on the statistical equilibrium should not depend severely on the type of frequency redistribution of line photons. The field-free results should therefore also be quite accurate when partial redistribution is used.

The basic problem of combining partial redistribution with Zeeman splitting is not solved by separating the formal Stokes vector solution from the statistical equilibrium computations. The wavelength dependence of the PRD line source function needs to be taken into account when writing the expression for the Stokes emission vector (RMD, Eq. 5, for the CRD case), but from the existing literature, all in terms of extremely tedious quantum-mechanical formalisms, it is not clear how this should be done. In Sect. 3.1 we explain the formalism that we use to cope with this problem and we indicate simplifications that may be used under certain conditions. We have implemented this PRD treatment in a formal Stokes vector solution routine (Sect. 3.2) and in subsequent sections we use this code to investigate the PRD effects on Stokes vector profiles of the Ca II K line formed in solar plage regions and the importance of velocities inside and outside the flux tubes.

In principle the line opacity is also affected by PRD, but that is only through stimulated emission, which is extremely small for the strong UV resonance lines considered here. We neglect this second order effect in the present analysis.

Other approximations made here that might not be valid are the neglect of atomic polarization, lateral radiative transfer and possible deviations from a Maxwellian velocity distribution. Considering the computational effort required to obtain the statistical equilibrium solutions with angle-dependent PRD, we feel that with current resources these approximations can only be dropped one at a time.

2. Angle-dependent PRD

2.1. Formulation

When macroscopic velocities are present in the atmosphere, angle-averaged partial redistribution functions no longer provide a good description of the scattering processes, since then there exists a correlation between the frequency of a scattered photon and the direction in which it travels. We therefore extended the angle-averaged PRD code of Hubený & Lites (1995), a modified version of Carlsson's (1986) MULTI code, to include the angle dependence of the redistribution function.

The general form of the redistribution function for converting a photon with frequency x' and direction $\boldsymbol{n}'$ into a photon with frequency x and direction $\boldsymbol{n}$, under the assumption of a sharp lower level, is

$$R(x', \boldsymbol{n}', x, \boldsymbol{n}) = \gamma R_{\mathrm{II}} + (1 - \gamma) R_{\mathrm{III}}, \tag{1}$$

where the redistribution function $R_{\mathrm{II}}(x', \boldsymbol{n}', x, \boldsymbol{n})$ (Hummer 1962) describes coherent scattering in the atom's frame with Doppler redistribution in the observer's frame, and $R_{\mathrm{III}}(x', \boldsymbol{n}', x, \boldsymbol{n})$ describes complete redistribution in the atom's frame. To good accuracy, R_{III} may be approximated by complete redistribution in the observer's frame, i.e.

$$R_{\mathrm{III}}(x', \boldsymbol{n}', x, \boldsymbol{n}) \approx \phi(x', \boldsymbol{n}') \phi(x, \boldsymbol{n}) \tag{2}$$

(Milkey et al. 1975; Vardavas 1976). This simplification does away with the very tedious evaluation of the R_{III} function (Reichel & Vardavas 1975; McKenna 1980).

The method of computing the angle-dependent redistribution function R_{II} is analogous to the one applied by Hubený & Lites (1995) for the angle-averaged case, which employs the spline description of Adams et al. (1971) in order to obtain sufficient accuracy in the evaluation of the scattering integral. The redistribution functions $R_{\mathrm{II}}(x', \mu', x, \mu)$ suitable for working on the (azimuthally-symmetric) angular quadrature of MULTI are obtained by taking the average of the function $R_{\mathrm{II}}(x', \boldsymbol{n}', x, \boldsymbol{n})$ over the azimuthal angle φ' of the absorbed photon:

$$R_{\mathrm{II}}(x', \mu', x, \mu) = \frac{1}{2\pi} \int_{0}^{2\pi} R_{\mathrm{II}}(x', \boldsymbol{n}', x, \boldsymbol{n}) \, \mathrm{d}\varphi', \tag{3}$$

where μ' and μ represent the direction cosines of the absorbed and emitted photons, respectively. This integration may be facilitated by noting that R_{II} is actually only a function of the absorption frequency x', the emission frequency x and the scattering angle θ:

$$R_{\mathrm{II}}(x', \boldsymbol{n}', x, \boldsymbol{n}) = \frac{g(\boldsymbol{n}', \boldsymbol{n})}{4\pi^2 \sin\theta} \exp\left[-\left(\frac{x - x'}{2}\right)^2 \csc^2\frac{\theta}{2}\right] \times$$
$$H\left[a \sec\frac{\theta}{2}, \frac{x + x'}{2} \sec\frac{\theta}{2}\right], \tag{4}$$

where $g(\boldsymbol{n}', \boldsymbol{n})$ is the angular phase function, for which we take the dipole phase function

$$g(\boldsymbol{n}', \boldsymbol{n}) = \frac{3}{4}(1 + \cos^2\theta), \tag{5}$$

and $H(a, v)$ is the Voigt function. Integrations over the azimuthal angle φ' of the directions of the absorbed photons may therefore be replaced by integration over scattering angle θ, provided suitable weight functions and integration intervals are used. Careful renormalization is required thereafter to avoid spurious photon sinks and sources. As noted by Milkey et al. (1975) it would probably be more accurate to also average R_{II} over appropriate intervals around each angle-quadrature value μ'_j instead of using only the grid values themselves. In the case of depth-independent redistribution functions that is easily done, but in the present case, with depth-dependent redistribution functions, that would require prohibitive amounts of computing time.

A completely analogous approach is taken for the evaluation of the generalized redistribution function P_{II} that is used to describe the cross-redistribution from another line into the line that is being considered. This approach differs from the one of Hubený & Lites (1995) in the angle-averaged implementation, since we found that using a denser frequency grid for the integration of the cross-redistribution part of the scattering integral is not accurate enough for angle-dependent cases.

The radiative transfer computations proceed in the way described by Hubený & Lites (1995), who implemented the method of Hubený (1985b): the PRD effects are computed within the equivalent two-level atom formalism and they couple to the rest of the atom through a single frequency- and direction-dependent parameter $\rho(x, \mu) \equiv \psi_{ji}(x, \mu)/\phi_{ij}(x, \mu)$, i.e. the ratio of the emission and absorption profiles. For given populations n_i we solve for

$$\rho(x, \mu) = 1 + \frac{n_i B_{ij}}{n_j P_j} \left[\bar{R}_{iji}(x, \mu) - \bar{J}_{ij}\right]$$
$$+ \sum_{l<j} \frac{n_l B_{lj}}{n_j P_j} \left[\bar{P}_{lji}(x, \mu) - \bar{J}_{lj}\right]. \tag{6}$$

Of particular importance, in the light of the Feautrier method used in MULTI, is the relation between $\rho(-x, -\mu)$ and $\rho(x, \mu)$, or, equivalently, between $\bar{R}_{iji}(-x, -\mu)$ and $\bar{R}_{iji}(x, \mu)$ (and between $\bar{P}_{lji}(-x, -\mu)$ and $\bar{P}_{lji}(x, \mu)$). Both may be expressed in terms of sums and differences of the redistribution functions and intensities:
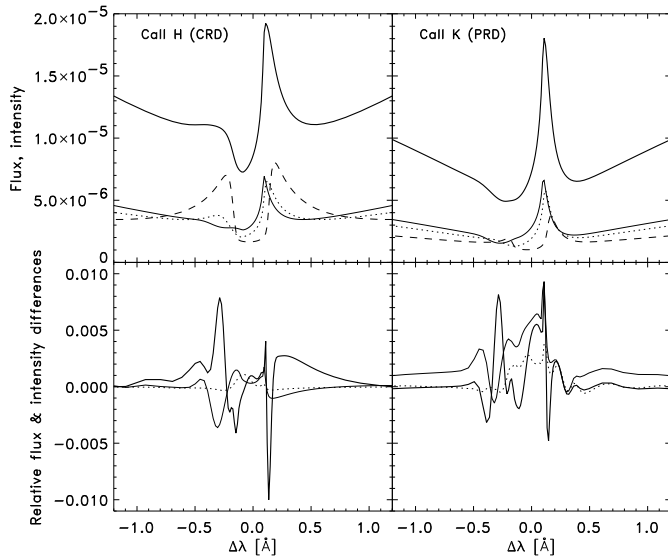
$$\bar{R}_{iji}(x, \mu) \equiv \frac{1}{2\phi_{ij}} \int_{-\infty}^{\infty} \mathrm{d}x' \int_{-1}^{1} \mathrm{d}\mu' \, R(x', \mu', x, \mu) I(x', \mu')$$
$$= \frac{1}{2\phi_{ij}} \int_{-\infty}^{\infty} \mathrm{d}x' \int_{0}^{1} \mathrm{d}\mu' \left[R^+ u + R^- v\right] \tag{7}$$

and

$$\bar{R}_{iji}(-x, -\mu) = \frac{1}{2\phi_{ij}} \int_{-\infty}^{\infty} \mathrm{d}x' \int_{0}^{1} \mathrm{d}\mu' \left[R^+ u - R^- v\right], \tag{8}$$

where

$$R^{\pm}(x', \mu', x, \mu) = R(x', \mu', x, \mu) \pm R(-x', -\mu', x, \mu), \tag{9}$$

Fig. 1. Flux and intensity profiles (top row) for the Ca II H & K lines calculated in the presence of large velocity gradients for $n_\mu = 9$, where n_μ is the number of angle-quadrature points per hemisphere. The thick lines represent the flux profiles, the thin lines are for the intensities. Each line style corresponds to a different μ-value: solid, dotted and dashed represent $\mu = 0.89$, 0.50 and 0.11, respectively. The relative differences between the profiles calculated for $n_\mu = 3$ w.r.t. $n_\mu = 9$ are shown in the bottom row. The intensity differences at $\mu = 0.11$ are not shown, since they would exceed the scale of the plots. Differences up to 10% occur for such small μ, independent of whether CRD or PRD is used

and

$$u(x, \mu) = \frac{1}{2} \left[I(x, \mu) + I(-x, -\mu) \right] \qquad (10)$$

$$v(x, \mu) = \frac{1}{2} \left[I(x, \mu) - I(-x, -\mu) \right]. \qquad (11)$$

The fact that $\rho(-x, -\mu) \neq \rho(x, \mu)$ causes the line source function to be different for upward and downward directions and makes Feautrier formal solutions for the intensities impossible. Instead we use the short-characteristics method (see, e.g., Kunasz & Auer 1988, Auer & Paletou 1994).

2.2. Tests of the implementation

The lack of good reference computations makes it difficult to ascertain the validity of the angle-dependent PRD code. We therefore used the angle-averaged version, to some extent tested by Hubený & Lites (1995), as a certified starting point. Results for static atmospheres agreed to within the convergence accuracy (usually 1 in 10^4), and convergence itself occurs as fast as in the angle-averaged case.

Mihalas (1978, p. 451) notes that because the argument of the line profile function is $(x - \mu v_{\mathrm{los}})$ the accurate evaluation of the scattering integral in moving atmospheres imposes rather strict limits on the angle quadrature. That requirement is especially true in cases where simple quadrature sums are used. Note,
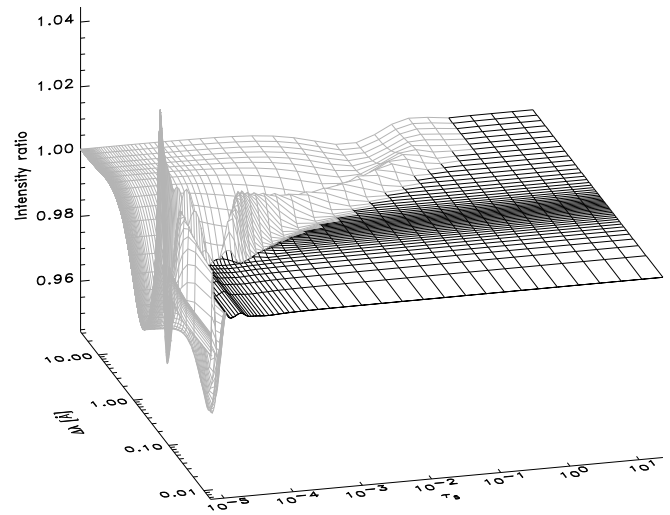
Fig. 2. Angle-averaged intensity ratio, $J_\nu(n_\mu = 3)/J_\nu(n_\mu = 9)$, as a function of optical depth at 5000 Å and as a function of wavelength from line center, for the Ca II H line computed with CRD. The boundary between the two differently shaded parts marks the monochromatic optical depth unity
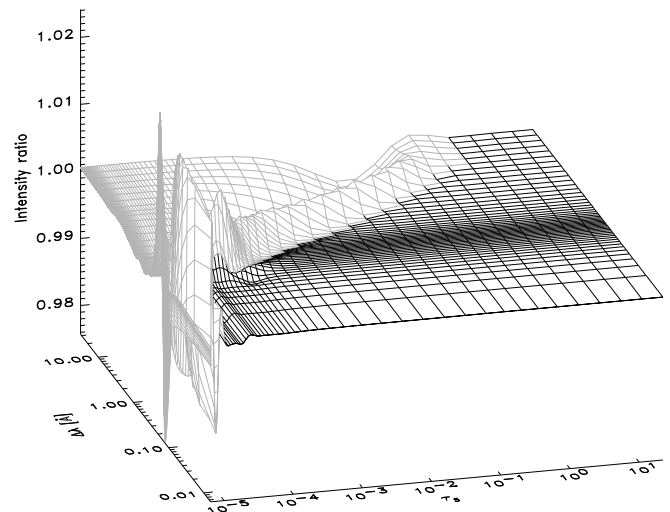
Fig. 3. Same as Fig. 2, but for the Ca II K line computed with PRD

however, that for the lines treated in PRD the scattering integral is not evaluated by means of a quadrature sum, but by means of the more accurate spline method of Adams et al. (1971). Since we intend to use the code on a variety of flow fields, we compared the results for angle quadratures with up to $n_\mu = 9$ angles per hemisphere, using the FAL-C quiet-Sun model atmosphere (Fontenla et al. 1991) with flow velocities up to 40 km/s at the Ca II K line's core formation height and large velocity gradients in the layers just below that. The fact that these velocities are large compared to values observed in the solar chromosphere is irrelevant here.

Fig. 1 compares the flux and intensity profiles of the (CRD) Ca II H and (PRD) Ca II K line profiles, computed with 3 and

9 angle-quadrature points. These computations have been done with PRD for the K line only, and cross-redistribution has been neglected; this provides results that incorporate the most important partial redistribution contribution to the K line and at the same time allows comparison with a similar line treated with complete redistribution without significantly compromising the non-LTE statistical equilibrium solution. Although no computations have been carried out with even larger numbers of angle-quadrature points, the additional comparison with results for $n_\mu = 6$ indicates that $n_\mu = 9$ may be assumed to give exact results in the context of this comparison. The differences between the flux profiles computed with 3 and 9 angle grid points are small, of the order of a percent or less, and there is no significant difference in accuracy between CRD and PRD. The differences between the intensity profiles for the smallest μ-value have not been included: they reach values up to 10% which would completely exceed the scale of the figure; it is for this reason that the flux differences are larger than the intensity differences at larger μ.

Similar differences occur in the line opacities (i.e. lower level populations) and line source functions, which are more fundamental parameters, but since both are angle-dependent they are difficult to compare when the number of angle-quadrature points is changed. However, since the line source function is mostly due to scattering, they are also easily revealed in a plot of the angle-averaged intensity J_ν as a function of optical depth in the atmosphere and wavelength from line center (Figs. 2 and 3). This demonstrates that for each wavelength $J_\nu(n_\mu = 3)$ and $J_\nu(n_\mu = 9)$ start to deviate from each other near monochromatic optical depth unity. As a consequence of the low weight of the wing parts, the deviations there, which occur already deep in the atmosphere, are of little significance to the parts of the line that are still optically thick.

These tests show that the number of angle-quadrature points is not as critical as one would initially expect. However, this statement holds for the radiative transfer computations of the lines only. The bound-free transitions, shortward of 1420 Å, which in the above computations have been given fixed rates (prescribed through a radiation temperature), would exhibit significant changes if they had been computed in full detail. The reason for those differences lies in the difficulty of describing the angular dependence of the radiation field at shorter wavelengths by means of only three quadrature points: the steep limb brightening very close to the limb is largely missed by such a coarse grid. This is a general problem that occurs for any type of radiative transfer computation in which the radiation at shorter wavelengths plays a role. Since this has nothing to do with the PRD computations themselves, although most of the results presented suffer from this inadequacy, we will continue to ignore it. This has little consequence for the conclusions drawn from those computations because most of those will pertain to differential experiments which are less sensitive to this type of inaccuracy. One has to keep in mind, however, that it may not be safe to ignore this inaccuracy when comparing computed profiles with observations.

3. PRD Stokes vector solution

3.1. Formulation of principles

Stokes vector formal solution routines generally assume that the magnetic sub-states of a level are equally populated, i.e. that there is no level polarization (complete level dealignment). The only means to guarantee this population equality is through a sufficiently high collision rate, although a lower collision rate will not necessarily mean that population equality is a bad approximation. These collisions, however, are the same type of 'elastic' collisions that are responsible for line broadening and frequency redistribution, which means that if there are sufficient collisions to assure population equality, PRD should be negligible as well. In this sense there remain some inconsistencies in the procedure outlined here to compute magnetically split line profiles with PRD under the assumption of population equality of the magnetic sub-states.

Recall (RMD, Eq. 5) that in the case of complete redistribution the expression for the emission vector $\boldsymbol{j} = (j_I, j_Q, j_U, j_V)^{\mathrm{T}}$ is

$$\boldsymbol{j} = \kappa_c S_c \boldsymbol{e}_0 + \kappa_0 S_L \boldsymbol{\Phi} \boldsymbol{e}_0. \tag{12}$$

The expression for the first component of this vector,

$$j_I = \kappa_c S_c + \kappa_0 S_L \phi_I, \tag{13}$$

with ϕ_I given by

$$\phi_I = \frac{1}{2}\phi_p \sin^2\gamma + \frac{1}{4}(\phi_b + \phi_r)(1 + \cos^2\gamma), \tag{14}$$

as well as the ones for the other Stokes emission vector components, contains factors of the type $\phi_j S_{\mathrm{L}}$, where $j = \{b, p, r\}$ stands for each of the basic polarization states and in which only the ϕ_j are frequency dependent; the CRD line source function S_{L} is frequency independent.

Thinking along the lines of Zeeman splitting causing a spectral line to be divided into three components (with different polarization states) that may be treated as separate lines, one can think of three different levels of sophistication to define the line emissivity in case the line source function is frequency dependent. We review all three, starting with the most detailed one and subsequently simplifying it to the most elementary form.

The three basic absorption components ϕ_j are composed of N_j Zeeman components, arising from transitions between magnetic sub-levels of the upper and lower level of the line and contributing to either ϕ_b, ϕ_p or ϕ_r depending on the ΔM value of the transition. Each Zeeman component has its own strength (or weight) S_{i_j} and magnetic-field-induced wavelength shift v_{i_j}. Following the notation of RMD (their Eq. 12) the generalized absorption profiles are

$$\phi_j(v) = \sum_{i_j=1}^{N_j} S_{i_j} H(a, v + v_{\mathrm{los}} - v_{i_j}), \tag{15}$$

where v_{los} accounts for the Doppler shift due to a possible line-of-sight velocity. All wavelengths are measured relative to the

line center and they are expressed in units of the Doppler width $\Delta\lambda_D$.

In case of complete frequency redistribution of line photons the line source function S_L is frequency independent, so that in the computation of the emission vector the appropriate addition of ϕ_j components to form $\phi_{I,Q,U,V}$ may be performed before multiplying by S_L. In case of partial redistribution the source term associated with each Zeeman component of the line has to be evaluated at the appropriate shift with respect to line center:

$$\phi_j S_j = \sum_{i_j=1}^{N_j} S_{i_j} H(a, v + v_{\mathrm{los}} - v_{i_j}) S_L(v + v_{\mathrm{los}} - v_{i_j}). \quad (16)$$

Omitting the background continuum contribution, the emission vector then reads

$$j_I(v) = \frac{1}{2}\kappa_0 \phi_p S_p \sin^2\gamma + \frac{1}{4}\kappa_0(\phi_r S_r + \phi_b S_b)(1 + \cos^2\gamma), (17)$$

$$j_Q(v) = \frac{1}{2}\kappa_0 \left[\phi_p S_p - \frac{1}{2}(\phi_r S_r + \phi_b S_b) \right] \sin^2\gamma \; \cos 2\chi, \quad (18)$$

$$j_U(v) = \frac{1}{2}\kappa_0 \left[\phi_p S_p - \frac{1}{2}(\phi_r S_r + \phi_b S_b) \right] \sin^2\gamma \; \sin 2\chi, \quad (19)$$

$$j_V(v) = \frac{1}{2}\kappa_0(\phi_r S_r - \phi_b S_b)\cos\gamma. \quad (20)$$

Consider now the first simplification. In case each of the ϕ_j is 'compact', i.e. if the constituting Zeeman components virtually coincide, there is no need to evaluate the line source function for each Zeeman component separately since the result will be virtually the same each time. In that case it is faster to determine the magnetic-field-strength-dependent center of weight position v_j of each ϕ_j,

$$v_j = \sum_{i_j=1}^{N_j} S_{i_j} v_{i_j}, \quad (21)$$

and to evaluate the line source function only once, namely at the wavelength $v + v_{\mathrm{los}} - v_j$. Then one can associate with the absorption component ϕ_j the source term

$$\phi_j S_j = \left(\sum_{i_j=1}^{N_j} S_{i_j} H(a, v + v_{\mathrm{los}} - v_{i_j}) \right) S_L(v + v_{\mathrm{los}} - v_j), \quad (22)$$

which can immediately be substituted in Eqs. (17)–(20) to obtain the emission vector. The line source function only needs to be evaluated at three positions in the line. This simplification is applicable for those cases in which the dispersion among the v_{i_j} values (for each j separately) is significantly smaller than the wavelength interval over which the line source function shows significant variation. It is obviously less suited to treat cases with the absorption components constituting each ϕ_j distributed over a wide range of wavelengths.

In case the magnetic splitting of the line is small compared to the wavelength interval over which the line source function markedly changes, i.e. all v_{i_j} values are small, an even simpler

approximation may be applied and the line source function only needs to be evaluated at one position in the line:

$$\phi_j S_j = \left(\sum_{i_j=1}^{N_j} S_{i_j} H(a, v + v_{\mathrm{los}} - v_{i_j}) \right) S_L(v + v_{\mathrm{los}}). \quad (23)$$

3.2. Implementation in the SPSR code

We have implemented the above method of including the wavelength dependence of the PRD line source function in its most general as well as in simplified forms in the Stokes Profile Synthesis Routines (SPSR), the formal Stokes vector solution code written by Murphy & Rees (1990). The straightforward correspondence between the coding in the routines and the description of the DELO method by Rees et al. (1989) significantly contributed to the ease with which this could be accomplished.

Except when performing very elaborate computations, where CPU time is really at a premium, there is no need to let the program decide whether or not one of the simplifications is valid. Therefore we decided to use separate options for the different degrees of sophistication of the PRD computation and explicitly specify which one to use through an input parameter. The essential modifications concern the input routine 'modin', which needs to read the wavelength-dependent line source function information obtained from a run with a PRD version of MULTI, and the routine 'abem', where the Stokes emission vector computation needs some modifications.

3.3. Comparison of PRD formalisms

Although for the present paper we only use the most detailed version of the PRD implementation, a comparison among the different options (including a detailed PRD computation, but using the wavelength-independent CRD line source function specified on a number of wavelength points analogous to the actual PRD source function) offers the possibility of eliminating coding errors and serves to assess how sensitively PRD influences the line profiles.

Fig. 4 shows a comparison of the Ca II K-line profiles for the different PRD options. It also includes the CRD profile which in the remainder of this paper means the formal Stokes vector solution obtained from the pseudo-CRD line source function that is based on the upper and lower level populations n_{u} and n_{l} from the PRD non-LTE computation. These populations, hence also the pseudo-CRD line source function, $S_L(CRD) = (2h\nu^3/c^2)/(n_{\mathrm{l}}g_{\mathrm{u}}/n_{\mathrm{u}}g_{\mathrm{l}}-1)$, differ slightly from the ones obtained with a fully consistent CRD Ca II computation.

The example shown in Fig. 4 is for the FAL-C (Fontenla et al. 1991) quiet Sun model and a magnetic field of $B = 3000\,\mathrm{G}$, with an inclination $\gamma = 45°$ and an azimuth angle $\chi = 15°$. All PRD options produce similar results, which significantly differ from the CRD profile. The very line core is unchanged in all Stokes parameters, as expected, since CRD is valid for the core formation. The K_1 and K_2 intensities are lower when PRD is used, but especially $dI/d\lambda$ is larger between K_1 and K_2, which is also reflected in the larger Stokes V values in those parts of
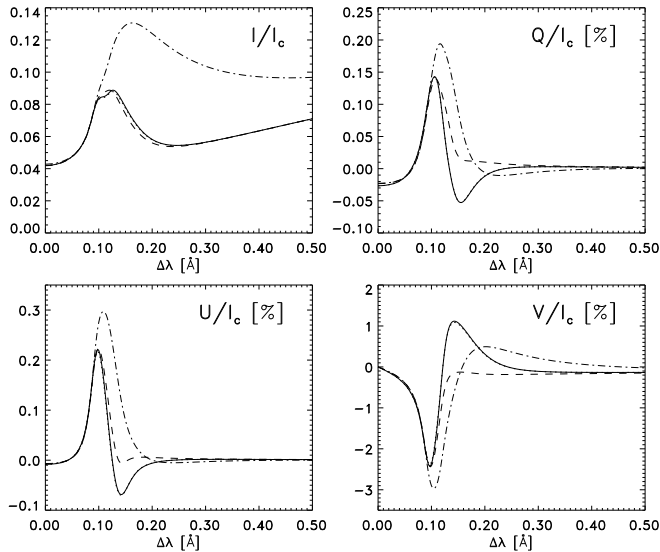
Fig. 4. Comparison of Stokes profiles (normalized to the continuum intensity I_c) of the Ca II K line computed with the different PRD options; the CRD profile (dot-dashed) is included for reference. The model atmosphere is the FAL-C quiet Sun model with a 3000 G magnetic field, inclined by $45°$ relative to the vertical line-of-sight. The field azimuth is set to $15°$ in order to also produce some Stokes U. The fully detailed PRD results (solid lines) and the results from using three source function components (dotted lines) virtually coincide; the results obtained with just one source function component (dashed lines) deviate too much to be useful for this line and field strength combination

the line. Otherwise, the Stokes V line shape remains roughly the same: PRD only modifies the size of the features already present in CRD. The Stokes Q and U parameters show somewhat more dramatic changes under the influence of PRD, since additional peaks appear. Also note the importance of magneto-optical effects: U is stronger than Q at this azimuth angle, whereas it would be weaker without magneto-optics.

As expected from the splitting pattern of the K-line the differences between PRD options 1 and 2 (detailed PRD and PRD with 3 source function components) are negligible (in the figure the dotted curves completely coincide with the solid ones), while option 3 (one PRD source function component) deviates significantly, indicating that the magnetic splitting is of the same order as the wavelength range over which the PRD line source function changes.

4. Ca II K in static FAL-C flux tube models

The Ca II K-line formation in a flux-tube atmosphere is complicated and depends on many intricately coupled parameters. As a first step to understand its behavior in such an environment we present computations for a simple, though not too unrealistic, flux tube model, constructed from the FAL-C quiet Sun model in the thin tube approximation. This atmosphere is used to model the interior of the rotationally-symmetric flux tube (for which FAL-C is a rather cool model) as well as its non-magnetic sur-
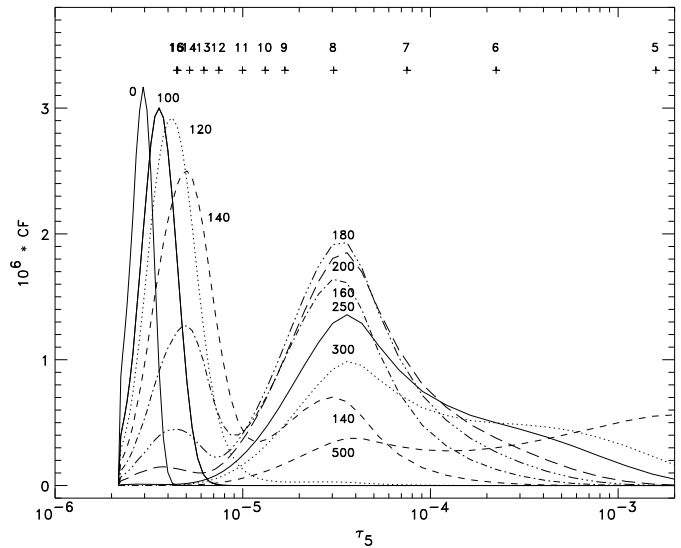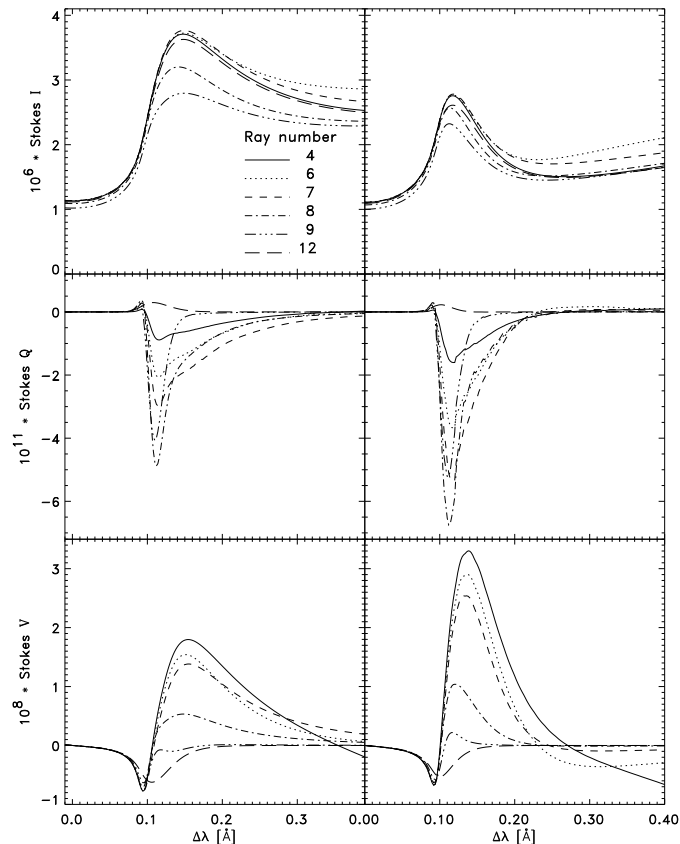
Fig. 5. Formation height of the Ca II K line in the FAL-C quiet Sun model atmosphere without magnetic field, using PRD. The curves represent the line intensity contribution functions at the indicated $\Delta\lambda$ (in mÅ) from line center. There is a fast transition from formation exclusively in the uppermost (magnetic) layer of the atmosphere for $\Delta\lambda \lesssim 100$ mÅ towards formation mainly in deeper layers for $\Delta\lambda \gtrsim 200$ mÅ. The crosses and numbers at the top indicate the height of the flux-tube boundary along the corresponding rays passing through the flux tube model

roundings; the two models are offset in height due to the Wilson depression resulting from the magnetic field inside the tube. The magnetic field has a typical strength of $B_0 = 1500$ G (at a height corresponding to standard continuum optical depth $\tau_5 = 1$ in the atmosphere surrounding the flux tube) and a low magnetic area filling factor $\alpha = 0.01$ (at that same height) is chosen to obtain a rather high-lying canopy. The statistical equilibrium is solved in 1-D plane-parallel fashion along a number of vertical lines-of-sight at different distances from the tube center. Along this sequence of rays the tube boundary height increases because the flux tube flares out laterally with height.

4.1. K-line formation height

The Ca II K-line formation spans such a large height range in the solar atmosphere that for realistic plage flux-tube models the very center of the line is formed almost completely within the magnetic canopy, whereas the wings are formed completely below the canopy along almost all rays (cf. Solanki et al. 1991). Most interesting are the intermediate parts of the line (i.e. wavelengths around K_1 and K_2) that sample both the magnetic canopy and the non-magnetic surroundings.

Fig. 5 shows the line intensity contribution function (Achmad et al. 1991; Solanki & Bruls 1994) for Stokes I of the K line formed in the FAL-C model atmosphere without a magnetic field. It provides a good indication where the different parts of the line are formed and in particular whether formation occurs in the magnetic or in the non-magnetic part of the atmo-
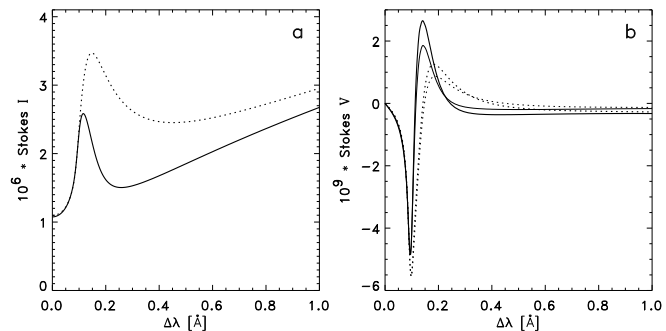
Fig. 6. Ca II K-line Stokes profiles from individual rays through the FAL-C flux-tube model. The distance from tube center increases with the ray number. The left column shows CRD profiles and the right one the corresponding PRD profiles

Fig. 7a and b. Spatially-averaged Stokes I and V of the Ca II K line. The solid curves represent the PRD profiles and the dotted ones the CRD profiles. Averages for Stokes Q and U are meaningless in this case. In **b** the thick curves represent the computed Stokes V profiles and the thin curves the corresponding $-\mathrm{d}I/\mathrm{d}\lambda$

tion in the non-magnetic surrounding atmosphere on the outer rays. The strength of the Ca II K line in combination with the small transverse magnetic field in the upper atmosphere produces extremely small and rather noisy solutions for Stokes Q and even more noisy ones for U, which in this case is only due to magneto-optical effects. Due to their weakness Stokes Q and U have little significance as observable parameters. For this reason, Stokes U will be omitted from the comparison.

The general behavior of the line profile as a function of distance to the tube center (increasing with ray number) is similar for PRD and CRD profiles, so that the incorporation of PRD in the computations may not provide additional diagnostic tools. The Stokes Q and V amplitudes are somewhat larger for the PRD profiles than for the CRD profiles. Especially between the K_1 and K_2 wavelengths, where, due to the onset of coherent scattering the PRD line source function drops significantly below the corresponding CRD value, Q^{PRD} approaches zero faster than Q^{CRD}. The dependence of the profile on distance to tube center is best understood by considering Stokes V, which qualitatively mirrors the behavior of the I profile following the weak field approximation ($V \propto \mathrm{d}I/\mathrm{d}\lambda$), but deviates significantly because the field strength varies with height in the atmosphere and drops to zero when crossing the tube boundary. Note that along any single ray even the magnetic flux is not height-independent. Magnetic-flux conservation is only fulfilled over the whole flux tube, i.e. when considering profiles averaged over all rays. Stokes Q closely follows the behavior of V, except that the relative amplitudes of the profiles formed along the different rays is different due to the opposite sensitivity of Q on magnetic field inclination.

- Close to tube center (rays 1–5) most of the line is formed within the magnetic part of the atmosphere, resulting in a small negative V peak between K_3 and K_2 and a larger positive V peak between K_2 and K_1; V becomes negative again beyond K_1. The relative amplitudes of the peaks in V to a large extent reflect the significant depth dependence of the magnetic field strength and flux.

sphere on a particular line-of-sight in a FAL-C flux tube model. Fig. 5 shows that for wavelengths not too far from line center, in particular the region around the K_2 peaks, the formation region lies in the magnetic part of the atmosphere on the rays close to tube center and in the non-magnetic surrounding atmosphere on more distant rays. The very line center, however, is nearly always formed in the magnetic canopy, whereas the wing parts beyond 500 mÅ from line center are nearly always formed in the non-magnetic surroundings. These three different regimes of formation are responsible for the richness of the Ca II K-line profiles revealed in the following sections, both from separate lines-of-sight as well as after spatial averaging.

4.2. Different vertical lines-of-sight

The schematic FAL-C flux-tube model serves to demonstrate the line profile changes caused by the increase of the tube boundary height with distance from the flux-tube center. Fig. 6 shows a comparison of CRD and PRD Stokes profiles for selected rays through the FAL-C tube model. The rays included are the most interesting ones from a radiative transfer point of view since the formation region of the part of the line around K_2 passes from the magnetic canopy on the inner rays to forma-

- At larger distances from tube center the tube boundary is located higher and an increasing part of the line wings is formed in the non-magnetic atmosphere below the tube boundary. First the negative V peak beyond K_1 disappears (rays 7–8) and eventually also the positive V peak between K_1 and K_2 is eliminated (rays 9–10).
- Far from tube center (rays 10–16) only the small negative V peak very close to line center that is due to the weak canopy field remains. Other parts of the line no longer pick up the magnetic field and remain unpolarized.

Given these properties, the relative strength of the peaks in the spatially-averaged V profiles in Fig. 7b could provide a (complicated) measure for the magnetic filling factor, which to a certain extent determines the canopy height. The basic distinction between CRD and PRD profiles, the narrower K_2 of the latter, is evident for all components of the Stokes vector on any individual line-of-sight as well as in the spatial average, suggesting that the PRD profiles will be more sensitive to velocities in the atmosphere.

Note that since magnetic flux is conserved with height when averaging over the whole flux tube (which is not the case along separate rays) the spatially-averaged V profile (Fig. 7b, thick curves) is much closer in shape to $dI/d\lambda$ (Fig. 7b, thin curves) than the Stokes V profiles of individual rays. The $dI/d\lambda$ curves in Fig. 7b have been normalized such that their maximum amplitudes equal those of the corresponding Stokes V profiles, so that $dI/d\lambda$ and Stokes V coincide in the central part of the line. Especially from the K_2 peaks outward $dI/d\lambda$ deviates from Stokes V; these differences may be attributed to the fact that the weak-field approximation may be expected to be correct for a height-independent magnetic field only. Only a minor fraction of the differences between V and $dI/d\lambda$ is due to not ideal sampling of the flux-tube structure by the 16 lines-of-sight, as we tested using 30 lines-of-sight. Note that the difference in relative strength of the negative and positive V lobes (in e.g. the long-wavelength half of the line) between profiles calculated along any ray (Fig. 6) and the averaged profile (Fig. 7b) shows that the V profile of this line can be used as a diagnostic of gradients of magnetic flux along the line-of-sight. This could have interesting applications for the determination of the vertical magnetic field strength gradient in spatially resolved magnetic features such as sunspots.

4.3. Inclined lines-of-sight

PRD effects are strongest in the tenuous upper atmosphere — the coherence fraction typically reaches maximum values of about 0.9 slightly above the temperature minimum (Uitenbroek 1989, Fig. 2) — and can thus be seen more easily in line profiles from slanted lines-of-sight. A detailed computation for the flux-tube model described above would be prohibitively time-consuming, since the azimuth-symmetry is broken for inclined lines-of-sight, requiring a 2-D grid of rays covering the entire tube area and including effects of rays traversing several tubes (e.g. Bünte et al. 1993). The present Stokes profile computations are restricted to a simpler geometry. They utilize the magnetic
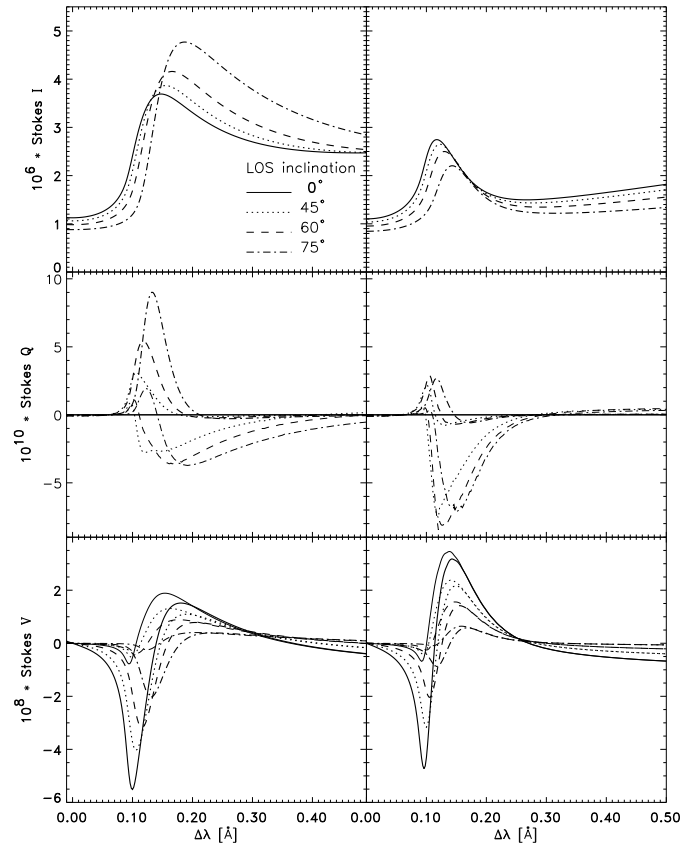
Fig. 8. Ca II K Stokes profiles for line-of-sight inclinations γ_{LOS} (measured from vertical) varying from 0 to 75 degrees and for two magnetic field stratifications, resulting from imposing a magnetic field strength, B_{top}, of 15 G (thin lines) and 120 G (thick lines), respectively, in the part of the atmosphere above the traditional merging height. The Q-profiles for $B_{top} = 15$ G have been enhanced w.r.t. the $B_{top} = 120$ G profiles by an additional factor of 10. The left column shows CRD profiles and the right column the corresponding PRD profiles

field stratification and the resulting line source functions and opacities from the (vertical) tube-center ray in a plane-parallel sense when obtaining line profiles for inclined lines-of-sight. They do, however, properly account for projection effects of the optical depth scale and the magnetic field vector. This is not a realistic approach for the line wings, which in reality mostly sample the non-magnetic surroundings of the tube anyway, but for the central part of the line this approach works well. For larger filling factors it becomes adequate for increasingly larger wavelengths (from line center). Note that in this simple model magnetic flux is not conserved with height. Hence we expect the K-line V and Q shapes to react sensitively to the magnetic field strength gradient.

Due to the azimuthal symmetry of the flux tube spatially-averaged disk-center profiles are subject to severe cancelation in Stokes Q and U. Using an inclined line-of-sight removes the azimuth-symmetry that previously caused the spatially-averaged Stokes Q and U to be meaningless.

The Stokes I profiles in Fig. 8 display the well known differences in center-to-limb behavior between CRD and PRD profiles; see e.g. Uitenbroek (1989) for an explanation in terms of optical thicknesses of the chromosphere and the temperature minimum region.

Changes in the line-of-sight inclination γ_{LOS} affect the Stokes V profiles in two ways. First, the decreasing strength of the longitudinal magnetic field acts similarly on CRD and PRD profiles: the strength of the positive V peak, located between K_1 and K_2, follows the $\cos\gamma_{LOS}$ relation very closely. The second works differently for CRD and PRD: towards the limb K_2^{CRD} (in Stokes I) becomes more prominent and its flank towards line center steepens, whereas K_2^{PRD} roughly maintains shape and size. As a result the strength of the negative V peak, located between K_2 and K_3, closely follows the $\cos\gamma_{LOS}$ relation in the case of PRD but decreases more slowly as a function of γ_{LOS} in case of CRD. The negative V peak is much more sensitive to the magnetic field strength in the upper layers of the atmosphere, than the positive peak. In the original 2-D model, of which we only consider the flux-tube interior, it is changes of α that mainly affect B_{top}, the field strength at the flux-tube merging height and above. Basically, the comparison between the two sets of computations shows the sensitivity of the Ca II K V and Q profiles to the vertical stratification of the field strength. Additionally, minor changes occur due to the slightly modified $B(\tau_\nu)$ relation resulting from projection effects.

The Stokes Q profiles, slightly noisy and with small amplitudes even for strongly inclined lines-of-sight, show different behavior under the influence of changing B_{top} and γ_{LOS}. The non-linear relation between Q and B (almost quadratic, as expected from the weak-field limit) is clearly visible in the innermost part of the line when comparing the profiles for $B_{top} = 15\,G$ and $B_{top} = 120\,G$ (note that the Q profiles for $B_{top} = 15\,G$ have been multiplied by a factor of 10). Roughly between line center and K_1 the Q^{PRD} and Q^{CRD}-profiles mimic the center-to-limb behavior of the corresponding I profiles: towards the limb the positive Q^{CRD} peak increases in strength and moves away from line center, whereas the negative Q^{CRD} peak and both Q^{PRD} peaks mainly shift in wavelength and do not change in strength significantly. This can be understood in terms of the optical thickness (at a particular wavelength) of the part of the atmosphere where the line source function follows the chromospheric temperature rise.

5. Sensitivity to model atmosphere parameters

In order to investigate in more detail the model dependences of the Stokes parameters of the Ca II K line we synthesized Stokes profiles, at vertical incidence, for a set of flux-tube models with magnetic filling factors α ranging from 0.01 to 0.16. For the tube component we used the FAL-F or FAL-P model of Fontenla et al. (1991), which are representative of a bright network area and a plage region, respectively. For the surrounding atmosphere we used the FAL-C quiet Sun model and in addition FAL-X, a more recent model by Avrett (1995) (his model M_{CO}) that has lower temperatures and densities in the upper photosphere and
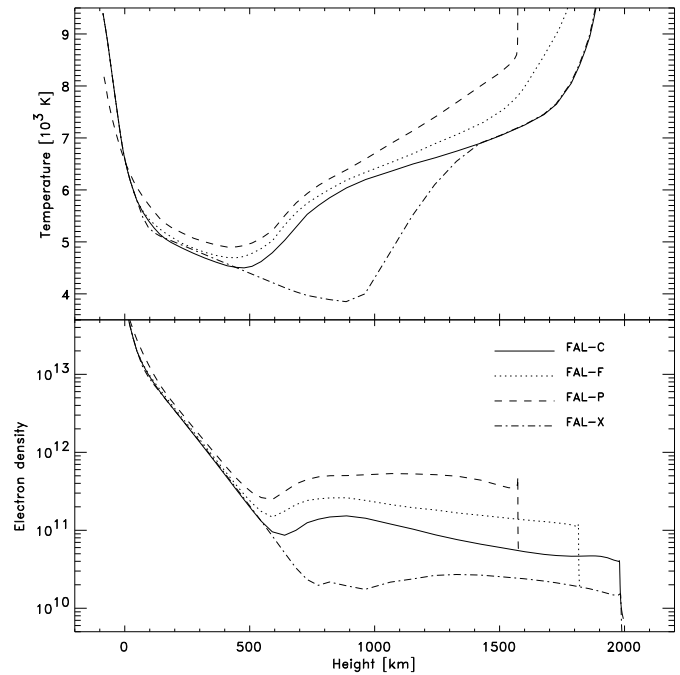

Fig. 9. Temperature and electron density vs. height for the four FAL model atmospheres. Each model is given on its own height scale, defined such that $h = 0$ at $\tau_5 = 1$

lower chromosphere and that was derived by fitting a large set of infrared CO-line observations (Farmer & Norton 1989). The temperature and electron density stratifications of these models are compared in Fig. 9.

The Stokes I and V profiles for the four model atmosphere combinations display similar ray-to-ray behavior as described above for the FAL-C tube model. The only significant differences are the relative amplitudes of the various peaks and the absolute polarization levels. Since the flux tubes cannot be spatially resolved in the observations we will limit ourselves to describing in some detail the differences among the computed spatially-averaged Stokes I and V profiles.
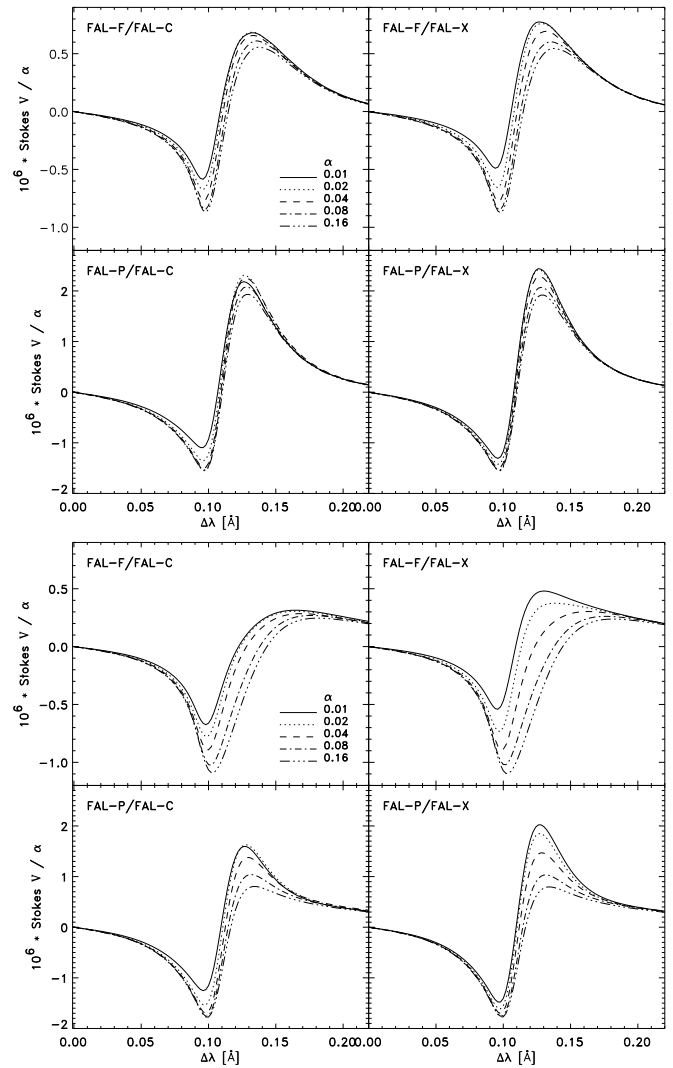
First of all, Fig. 10 shows that the CRD and PRD Stokes I profiles display the same behavior for the current set of model atmospheres and magnetic filling factors. The strength of K_2 — amplitude as well as width — increases with α. This is obvious since in addition to the increase of the area fraction covered by the flux tube at a fixed height, the canopy height decreases when α increases, so that the hot tube chromosphere is felt more strongly by the K line. At larger filling factor values the merging height drops so far that the differences between the FAL-C and FAL-X surrounding atmosphere models are no longer noticeable in the spatially-averaged line profiles; only the significant differences between the FAL-F and FAL-P tube models stand out. As expected, the largest K_2 amplitudes are obtained for the combinations with the (hotter) FAL-P tube component and the choice of the model atmosphere for the non-magnetic surroundings makes a smaller difference to the K_2 amplitudes.
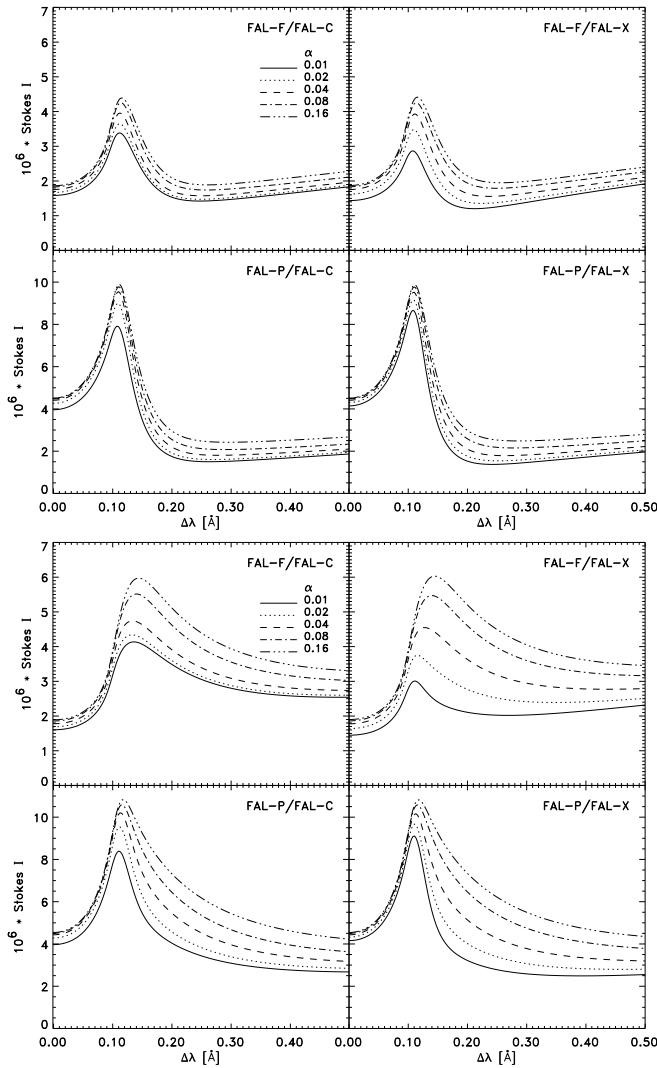
Fig. 10. Spatially-averaged Ca II K Stokes I profiles for the FAL-F/P $\times$ FAL-C/X flux-tube models, as indicated. The top half of the figure shows the PRD profiles and the bottom half shows the corresponding CRD profiles. The various line styles represent the different filling factors. Note the scale difference between the results for combinations with FAL-F and combinations with FAL-P

Fig. 11. Scaled spatially-averaged Ca II K Stokes V profiles for the FAL-F/P $\times$ FAL-C/X flux-tube models, as indicated. The top half of the figure shows the PRD profiles and the bottom half shows the corresponding CRD profiles. The V profiles in each panel have been divided by the respective filling factors to accentuate the line profile shape changes rather than the changes in the amplitude. Note the scale difference between the results for combinations with FAL-F and combinations with FAL-P

The primary effect of increasing the filling factor is to increase the relative volume filled by the flux tube. Hence for increasing filling factor the I profile of the K line changes from being similar to a quiet-Sun (or external atmosphere) profile to being practically a pure flux-tube line profile. This change is expected to be larger if the thermal contrast between the flux tube and surroundings is larger. Although the profiles resulting from the FAL-F flux tube follow the expected trend, the profiles from the FAL-P flux tube exhibit the opposite behavior. Responsible for this at first sight counter-intuitive behavior is the dependence of the merging height on filling factor and temperature.

Starting from the highest filling factor value, the merging height increases when α decreases; this increase is slower when the temperature difference between the tube and its surroundings

is larger (Solanki & Steiner 1990), i.e. hotter tubes (FAL-P) and cooler surroundings (FAL-X) cause a slower rise of the merging height. At $\alpha = 0.01$ the models with the FAL-P tube component have their merging height roughly 100 km lower than the corresponding models with a FAL-F tube component; the models with the FAL-X tube surroundings have their merging height roughly 200 km lower than the models with the FAL-C surroundings. For the models with the FAL-P flux-tube component the merging height at all filling factors is so low that K_2 is formed mainly above it, resulting in a small dependence of K_2 on the filling factor (note that K_1 varies just as strongly with filling factor as for the FAL-F flux tube). The low merging height

for the FAL-X external model means that even for $\alpha = 0.01$ the K_2 peak differs only little from that produced by FAL-P.

Only in the innermost part of the line the Stokes V profiles (Fig. 11) display deviations from a simple scaling with α. This simple scaling would hold throughout the entire line in the ideal case that filling factor changes would only result in proportional magnetic field changes, without any differences in other parameters. However, K_2 emission in Stokes I increases due to the hotter tube chromosphere while the canopy height decreases when α increases. These effects also influence Stokes V: the differences are such that growth of the negative peak with increasing α (i.e. increasing field strength at the height where this part of the line is formed) causes the positive peak to decrease in strength, as expected from the behavior of $dI/d\lambda$. Unfortunately, these changes appear not so large that they could be used as an accurate merging height diagnostic.

Clearly, however, the dependence of amplitude and form of the PRD I and V profiles (the latter after division by the respective filling factor) on the filling factor is much smaller than that of the CRD profiles. We expect that this is due to the fact that coherent scattering more easily relays information over larger distances in the atmosphere, so that the deeper onset of the chromospheric temperature rise in models with larger filling factor is less strongly reflected in PRD profiles than in CRD profiles.

6. Ca II K in plage flux tubes with velocities

Solar plage and network regions are highly dynamic features and one does not expect static models to produce line profiles that show all the characteristics of the observed profiles. In particular, the omnipresent asymmetry (read: deviation from perfect anti-symmetry) of Stokes V profiles — photospheric lines in general have a stronger blue part near solar disk center — has given rise to widespread speculation concerning its nature. In particular, observations of the K line have revealed highly asymmetric V profiles (Martínez Pillet et al. 1990).

Normally, lines as wide as Ca II K are less sensitive to velocities than narrow lines, but since the K line's most eminent features, the K_2 peaks and their Stokes V signature, have widths comparable to those of typical photospheric lines, it may be expected that the K_2 features have a similar velocity sensitivity as a normal narrow spectral line. We also expect differences between the PRD profiles and the CRD profiles, which have significantly wider K_2 peaks. The narrower K_2 peaks of the PRD profiles make them not only more sensitive to velocity gradients, as we shall see in Sects. 6.2 and 6.3, but also to turbulent velocity (Uitenbroek 1989). For the correct determination of the turbulent velocity in magnetic features, PRD effects acting on the Stokes profiles must be taken into account.

The basic difference between the CRD and PRD profiles, also responsible for the sometimes peculiar shape of the PRD line profiles, is the underlying line source function. The CRD source function is independent of wavelength and it follows the chromospheric temperature rise to high layers in the atmosphere. The PRD source function behaves similarly only in the
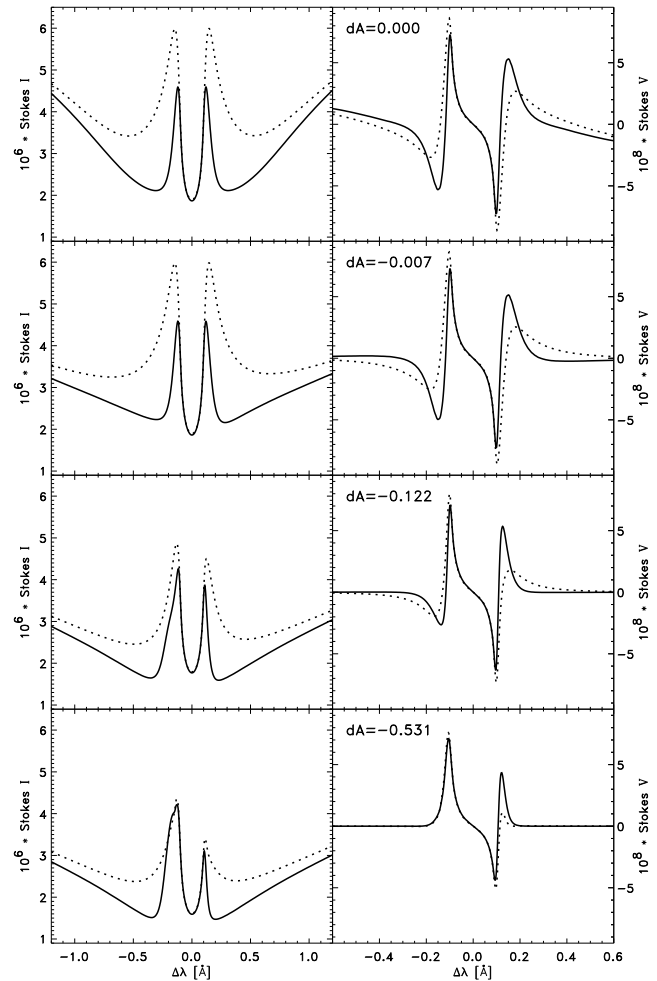
Fig. 12. Stokes I and V profiles for four vertical rays through the FAL-F/FAL-C tube model with zero velocity inside the tube and 5 km/s upflow in the surrounding atmosphere. The four rows represent four rays, for which the tube boundary heights are located at standard continuum optical depths $\log \tau_5 = -1.9, -3.3, -4.1$, and -4.6, corresponding to geometrical heights of 125, 325, 520, and 715 km, respectively. Solid curves represent the PRD profiles and the dotted ones represent the CRD profiles. Note the factor of 2 difference between the I and V wavelength scales. The Stokes V relative area asymmetry dA indicated in the right frames refers to the PRD profiles

line core, roughly within 100–150 mÅ from line center. Further from line center the effect of coherent scattering becomes appreciable and photons are lost more easily, depressing the line source function significantly. Noting that a velocity of 1 km/s produces a Doppler shift of 13 mÅ, it is clear that velocities of 5–10 km/s could produce significant changes in the line formation properties.

Due to the complexity of the Ca II K line profile we must distinguish here between two types of asymmetries. The first is the usually considerable asymmetry between the red and blue K_2 peaks. This asymmetry is also present in Stokes V (although to a greater or lesser degree, depending on the relation between the velocity gradient and the magnetic field). In addition, there
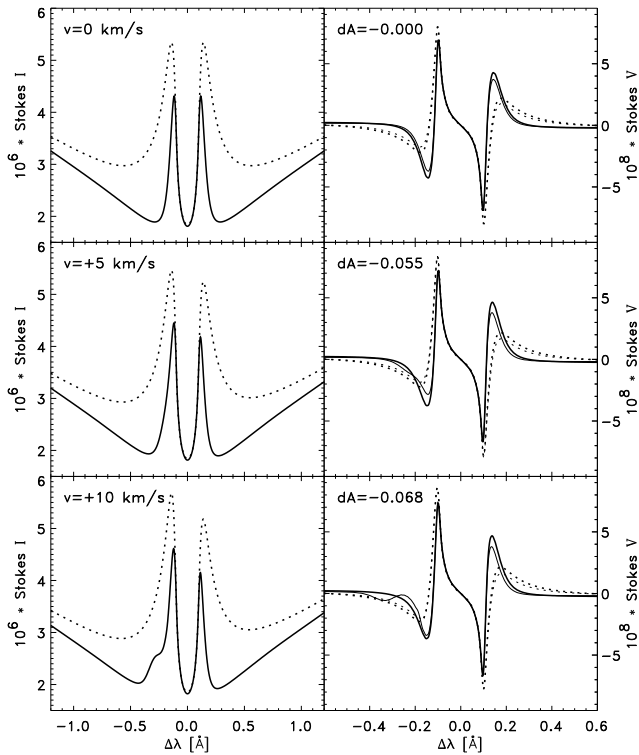
Fig. 13. Spatially-averaged Stokes I and V profiles for the FAL-F/FAL-C tube model with zero velocity inside the tube and from top to bottom 0, 5 and 10 km/s upflow in the surrounding atmosphere. Solid curves represent the PRD profiles and the dotted ones represent the CRD profiles. In the right column the thick curves represent the computed Stokes V profiles and the thin curves represent the corresponding $-dI/d\lambda$. Note the factor of 2 difference between the I and V wavelength scales. dA values of the PRD Stokes V profiles are indicated

is the asymmetry between the areas of the positive and negative lobes of Stokes V, which has no direct counterpart in Stokes I. Usually this Stokes V area asymmetry is taken between the blue (or violet) and red V lobes. Due to the complex form of the Ca II K V-profile, with two negative and two positive lobes in the central part of the line, we define the relative area asymmetry of Ca II K Stokes V as:

$$dA = \frac{(A_V(K_{2V}) + A_V(K_{2R})) - (A_R(K_{2V}) + A_R(K_{2R}))}{(A_V(K_{2V}) + A_V(K_{2R})) + (A_R(K_{2V}) + A_R(K_{2R}))}, \quad (24)$$

where A stands for an area and its indices (V or R) refer to the violet and red lobe, respectively, of the Stokes V signature of the indicated K_2 peak. This definition of dA is equivalent to the V area asymmetry definition by Martínez Pillet et al. (1990).

Coupled velocity and field-strength gradients are responsible for producing a non-zero dA. The sign of dA is given by

$$\text{sign}(dA) = \text{sign}(-\frac{d|B|}{d\tau}\frac{dv}{d\tau}) \quad (25)$$

(Solanki & Pahlke 1988; Sanchez Almeida et al. 1989). Although this relation was originally derived for simple absorption line profiles (in LTE), Figs. 15 and 16 will show it to be

valid also for the more complex case of the Ca II resonance lines if we use Eq. (24) to define dA and take velocity v positive when directed away from the observer. In addition, it has been shown (e.g., Grossmann-Doerth et al. 1988b; Solanki 1989; Bünte et al. 1993) that the zero-crossing wavelength is not shifted in case the gradients in B and v are spatially separated.

In the following we present the Ca II K Stokes I and V profiles for a few schematic flow fields in a flux-tube structure in order to obtain some insight into the velocity sensitivity of this very wide line. These are schematic in the sense that we always use the same models for the tube interior (FAL-F) and surroundings (FAL-C), employ a filling factor of 0.08, prescribe velocities as a function of height only (horizontal variation of velocities only occurs at the tube boundary), allow the mass conservation requirement to be violated and ignore correlations of temperature and velocity such as occur in granulation or in realistic shock waves.

In some of the following sections height-dependent velocity structures are used, which uncover an intricate problem with the geometrical height scales that has to do with non-LTE effects on the hydrogen populations. Even though we have non-LTE hydrogen populations for each of the input model atmospheres, after constructing lines-of-sight through their combination (in the thin-tube approximation) it is impossible to determine realistic non-LTE hydrogen populations at all heights without actually solving the 2- or 3-D radiative transfer and statistical equilibrium problem for the most important atomic species. Obviously, adopting the non-LTE population departure coefficients of either of the constituting model atmospheres will not make sense, since the modified geometry should result in different non-LTE departures in the combined model. Instead, we chose to use the LTE Saha-Boltzmann distribution of the total hydrogen number density throughout the entire model. The most important consequence of this choice is that the computed opacities per unit volume differ from the ones of the input models so that the geometrical height scale is significantly stretched towards the upper part of the atmosphere (roughly by a factor of two) with respect to the original non-LTE height scales of the FAL-F and FAL-C model atmospheres. This height scale stretching is most inconvenient for the model used in Sect. 6.3.

6.1. Zero velocity inside; constant velocity outside

Consider the simple case of a flux tube without any flow field embedded in a medium with height-independent upflow of 5 km/s. In this example we have chosen upflows outside the tube based on the fact that the flow in the outermost rays of the tube structure determines the asymmetries in the central part of the spatially-averaged profiles. This assumption is in agreement with the general picture that network flux tubes concentrate in the downflow areas of the atmosphere, the intergranular lanes and supergranular boundaries, with upflow regions located at larger distance, where the tube boundary is rather high. A similar argument holds for plage tubes embedded in (abnormal) granulation.

Fig. 12 demonstrates that this upflow is noticeable as an asymmetry in Stokes I and V only for the outermost rays, which
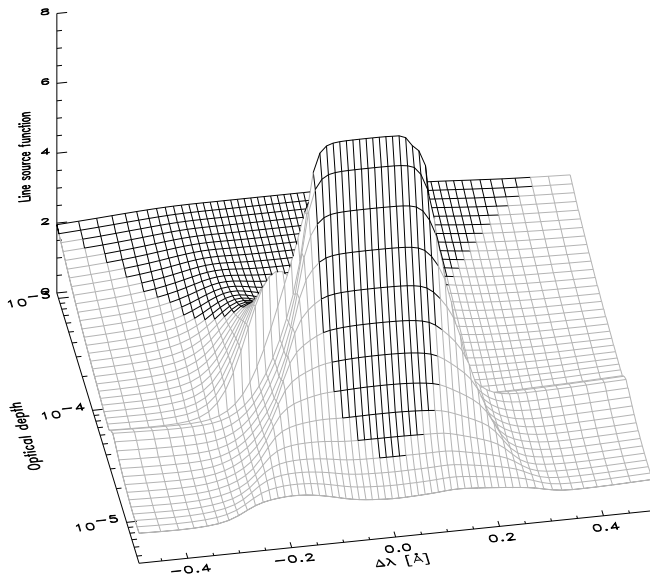
Fig. 14. PRD line source function vs. wavelength and standard continuum optical depth τ_5 for the central part of the Ca II K line in the upper part of the outermost ray of the flux tube model with a 5 km/s upflow in the surrounding atmosphere. The switch between the different shadings occurs at monochromatic optical depth unity

have rather high-lying tube boundary height. On those rays the tube boundary is located at such a height that for wavelengths close to line center (the only part of the line with non-negligible V strength) asymmetries in the line source function due to the velocity field in the underlying non-magnetic atmosphere are not completely washed out before the radiation escapes from the atmosphere. For the rays closer to tube center there is a wavelength shift in the line wings rather than an asymmetry in the core of Stokes I. Note that Stokes V calculated in PRD are significantly more asymmetric than the V profiles in CRD (both as far as K_{2V} vs. K_{2R} asymmetry and dA are concerned). We expect that this is a result of the larger sensitivity to velocity of the narrower PRD profiles.

The spatially-averaged profiles in Fig. 13, for upflow velocities in the surrounding medium of 0, 5 and 10 km/s, respectively, show only a hint of this asymmetry, unless the flow velocity is extremely high. These profiles extend the validity of the proposal by Grossmann-Doerth et al. (1988a) for producing unshifted asymmetric Stokes V profiles to the case of non-LTE line formation subject to PRD. The K_{2V} and K_{2R} peaks have different strengths and at larger velocities a bump develops between K_{1V} and K_{2V}. As expected for an upflow outside the flux tube, in Stokes V the red part of each K_2 feature dominates, in the sense that the area under $|V|$ is larger for the red part of both K_{2V} and K_{2R}. This corresponds to a negative dA. For a model with lower magnetic filling factor α the Stokes V signal will be weaker — the weak field approximation (thin curves in bottom row of Fig. 13) is fairly accurate here so that V will be proportional to α — but the weight of rays with high-lying tube boundary will be larger so that the asymmetry grows. This

suggests that the asymmetries introduced into Ca II K Stokes V profiles originating from network regions by velocities outside the flux tubes will generally be larger than of the plage profiles. It is expected, however, that other effects are more important in producing differences between plage and network profiles of Ca II K.
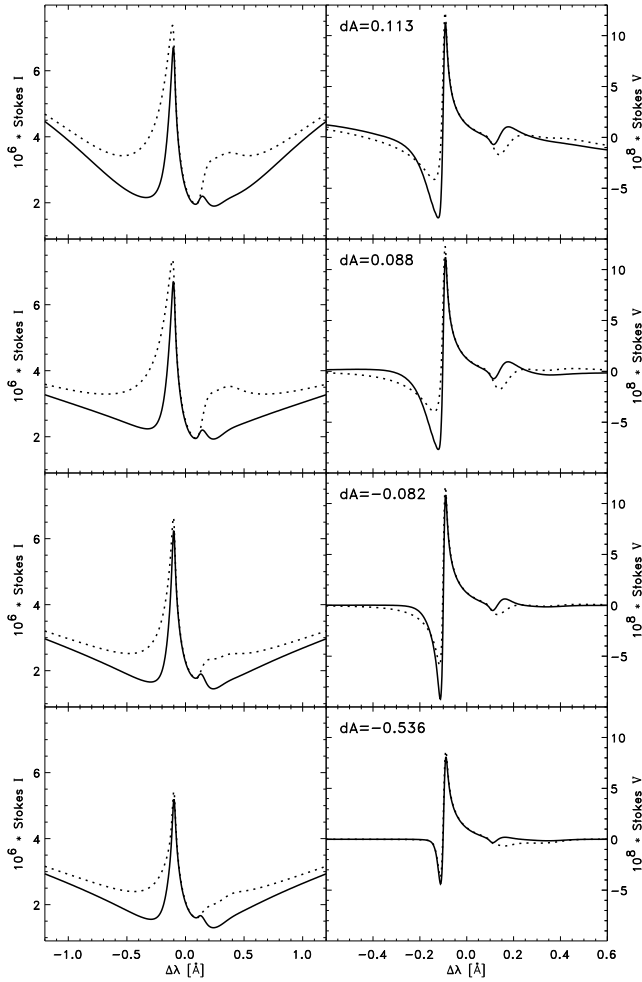
The CRD Stokes I profiles have less asymmetry than their PRD counterparts and the accompanying CRD Stokes V profiles are in most cases almost perfectly antisymmetric. Note the tendency for upflows outside the flux tube to produce Stokes I profiles in which K_{2V} is stronger than K_{2R}, the line wings are blue-shifted, and the red part of Stokes V is slightly dominant.

Fig. 14 provides a clear picture of what happens to the line source function in the central part of the line (on the outermost ray through the tube model with a 5 km/s upflow in the nonmagnetic part). The chromospheric line source function bump is a feature that is fixed to the wavelength of the line center, i.e. it exactly follows the flow velocities in the atmosphere. The constant blueshift of this line source function bump in the deeper parts of the atmosphere as plotted here as well as its sudden jump in wavelength when going into the static magnetic canopy are clearly visible. Depth variation of the flow velocity causes the monochromatic optical depth (i.e. line plus continuum) to change with respect to the static case, because the line opacity is moved around in a certain wavelength range. The line source function in combination with the optical depth information — the boundary between the differently shaded regions lies at monochromatic optical depth unity — provides a good idea of what the emergent line profiles look like. In this case the jump in the flow velocity occurs slightly deeper than where the K_2 peaks are formed, so that their Doppler shift is zero and the difference between the K_{2V} and K_{2R} shapes is very small. At larger flow velocities the wavelength jump at the tube boundary is larger, which increases the effects due to shifting around the line opacity. At lower filling factor values this jump occurs higher in the atmosphere, which also tends to increase the differences between the K_2 peaks.

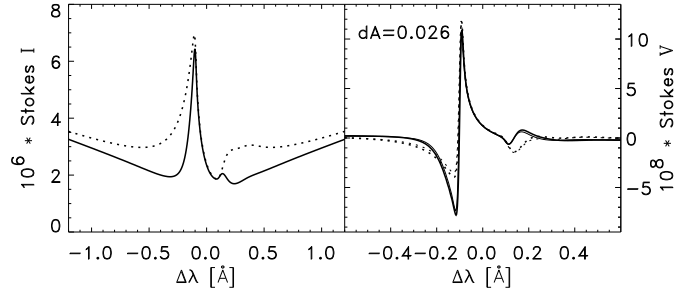### 6.2. Steady flow inside; zero velocity outside

In the photospheric layers of small flux tubes, strong downflows have been ruled out (Stenflo & Harvey 1985; Solanki 1986; Martínez Pillet et al. 1997). In the transition zone, however, downflows are pervasive (Doschek et al. 1976; Lites et al. 1976; Feldman et al. 1982), so that it is not unreasonable to consider the effect of downflows within magnetic elements on the Ca II K line.

Line profiles with similar shapes as those in Figs. 12 and 13 would be obtained with a height-independent flow in the opposite direction inside the flux tube and no flow outside the tube. This is so because the relative flow velocity of the matter inside the tube with respect to its surroundings is a much more relevant parameter than the absolute velocities, except for the wavelength shifts. Things completely change, however, when velocity gradients are present in the atmosphere.
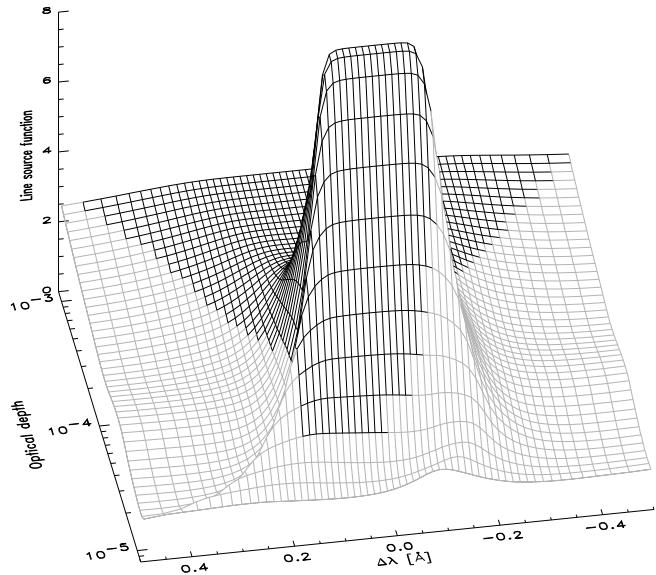
Fig. 16. Spatially-averaged Stokes I and V profiles for the FAL-F/FAL-C tube model with a steady downflow fulfilling mass conservation inside the tube and zero velocity in the surroundings of the tube. Solid curves represent the PRD profiles and the dotted ones represent the CRD profiles. In the bottom panel the thick curves represent the computed Stokes V profiles and the thin curves represent the corresponding $-\mathrm{d}I/\mathrm{d}\lambda$. Note the factor of 2 difference between the I and V wavelength scales. The dA value of the PRD V profile is indicated

Fig. 15. Stokes I and V profiles for four vertical rays through the FAL-F/FAL-C tube model with a steady downflow inside the tube and zero velocity in the surroundings of the tube. The four rows represent the same four rays as in Fig. 12, i.e. with the tube boundary heights at standard continuum optical depths $\log \tau_5 = -1.9, -3.3, -4.1,$ and -4.6. Solid curves represent the PRD profiles and the dotted ones represent the CRD profiles. Note the factor of 2 difference between the I and V wavelength scales. dA values of the PRD V profiles are indicated

Fig. 17. PRD line source function vs. wavelength and standard continuum optical depth τ_5 for the central part of the Ca II K line in the upper part of the central ray of the flux tube model with mass-conserving upflow inside the tube. The switch between the different shadings occurs at monochromatic optical depth unity

As an extreme example we consider a steady downflow in the tube (vertical velocities only): mass conservation determines the velocities at all heights in the atmosphere if we fix the flow velocity at some height. Prescribing a reasonable velocity of 5 km/s at $\tau_5 = 10^{-5}$, i.e. right in the formation region of the central part of the line, due to mass conservation leads to negligible velocities only two scale heights deeper and to very large velocities of up to 40 km/s where the line becomes completely optically thin. This presents a good example for cases with extremely large velocity gradients in this particular part of the atmosphere. This velocity stratification is also compatible with the unshifted Stokes V zero-crossing wavelengths of photospheric lines. Figs. 15 and 16 again present the I and V profiles for single rays and for the spatial average, respectively.

Now the profiles from all rays are very asymmetric in the sense that the K_{2R} peak and the corresponding signature in Stokes V are almost absent. This asymmetry is easily understood by looking at the behavior of the line source function near the line center in the upper part of the atmosphere (Fig. 17). The line source function surface itself is already asymmetric: the chromospheric bump that is normally symmetric around line center is increasingly redshifted towards the very top of the atmosphere due to the rather large velocities there, and the location of optical depth unity, which is significantly modified by the flow, stresses this asymmetry even more. Without invoking

a formal solver one can see from this plot that near the usual K_{2R} wavelength the line source function no longer rises dramatically in the region of monochromatic optical depth unity, whereas near K_{2V} the rise may even be stronger than without the flows.

In contrast to this marked asymmetry between K_{2V} and K_{2R} the dA of Stokes V is relatively small and the weak-field approximation is again quite good for estimating the spatially-averaged Stokes V profile. Also, whereas K_{2R} is negligible relative to K_{2V} for all rays, dA changes sign from the inner to the outer rays. In the model considered in the present subsection $dv/d\tau$ has the same sign (< 0) at all heights and along all rays. $d|B|/d\tau$, however, can change sign. Within the flux tube B decreases with height, i.e. $d|B|/d\tau > 0$, whereas at the flux tube boundary $d|B|/d\tau < 0$. For rays close to the flux tube axis the former gradient dominates, so that $dA > 0$, while at larger radii the boundary, which now lies higher, becomes more important, so that $dA < 0$ is produced along those rays. The small dA of the averaged profiles results from the cancelation of the dA from the individual rays.

Further computations show that additional flows in the surrounding atmosphere change the line profiles only very little, as already could have been guessed from comparing the current results with the ones for velocities in the surroundings (Sect. 6.1).

6.3. Moving shocks inside; zero velocity outside

A third velocity structure of practical interest consists of shocks that travel upward inside the flux tube. It is important to stress that the models used here are not thermodynamically consistent. In particular, shocks cause significant local heating of the atmosphere (e.g., Carlsson & Stein 1992), which is not taken into account in the current model. We simply use a train of shocks, or rather a saw-tooth-shaped flow velocity pattern, with shock separations of 500 or 1000 km and a maximum upflow velocity of 10 km/s. In this model there is no downflow present at any height, whereas in reality we generally expect strong downflows in the region immediately above the shock, and those are expected to contribute significantly to dA of the opposite kind as the one produced by the shock itself. The shock fronts are assumed to move upwards with constant velocity, so that independent of the actual propagation speed a full "wave period" can be sampled by moving the entire velocity structure up by 5 steps of 0.2 times the shock separation each.

In this section we will consistently refer to the shock separations as being 500 and 1000 km, but those refer to the distances when measured on a geometrical height scale computed from FAL-C (or FAL-F) non-LTE hydrogen populations. In reality, we used the LTE hydrogen populations for the radiative transfer computations and those tend to stretch the height scale by about a factor of two (as pointed out earlier), so that the shock separations actually turn out to be about 1000 and 2000 km.

Columns 1 through 5 of Fig. 18 show the spatially-averaged I and V profiles for each of the 5 "time steps" of a full wave period for shock separations of 500 and 1000 km, respectively, and the sixth columns show the corresponding "time averages".

Although the shocks themselves do not change in strength we find that a 1000 km shock separation produces more line profile asymmetries and changes in time than a smaller shock separation, whereas the time-averaged profiles come out remarkably similar. In effect, the time-averaged profiles should be almost identical, so that we expect that some of the differences between them are due to our incomplete sampling. Furthermore, from Fig. 18 we see that this type of velocity may produce various types of spatially-averaged line profiles: K_{2V} may be stronger than K_{2R}, but also significantly weaker, depending solely on the heights at which the shocks occur. The main effect of the shocks averages out when forming the time-averaged profiles, thus the remaining asymmetry of the Stokes I profile corresponds roughly to that produced by an internal upflow of 5 km/s. The Stokes V profile is considerably more asymmetric, however. It is noticeable that in spite of the extremely asymmetric profile shape the dA of the spatially-averaged V profile is relatively small. This is because in our model the jump in v at the location of the shock is not associated with a corresponding jump in B, so that dA is mainly produced by the jumps in B and v at the flux-tube boundary. This means that only the profiles from the outermost rays have larger dA values, since on those rays the flux-tube boundary lies in the formation region of the central part of the line.

Additional computations for a saw-tooth velocity structure ranging from -5 to $+5$ km/s, i.e. with a downflow above the shock, produce line profiles that differ from the ones in Fig. 18 only in details. The most important difference is that the line profile variation as a function of time (upward propagation) is out of phase by half a period, and that the Doppler shifts of the line core now also reflect the presence of downflows. The major shortcoming of these profiles as well as the profiles in Fig. 18 is that they don't show a large disparity between K_{2V} and K_{2R}, whereas solar observations show a dramatic dominance of K_{2V} in the form of bright grains. Most likely, the reason for this discrepancy is the absence in our models of a close correlation between temperature, density and velocity in the shock regions. Indeed, including such correlation in a consistent manner, Carlsson & Stein (1997) are able to match the observed behavior of individual H_{2V} bright grains.

For a given shock distribution the line profiles for all rays are very similar, i.e. they resemble the spatially-averaged profile, and to understand how the different line profiles come about, it suffices to look at the line source functions on a single ray through the tube models. The line source functions corresponding to the line profiles in the first and third row of the right part of Fig. 18 are shown in Fig. 19. The main difference between the velocities underlying the two panels is the 400 km offset in height of the shocks. In the first case (upper panel) there is a small flow velocity gradient in the inner wing formation region — the upward velocity increases linearly with height and reaches 10 km/s at about $\tau_5 = 2 \cdot 10^{-5}$ — followed by a shock (sudden decrease of the upward flow velocity to zero) near the top of the atmosphere. The velocity gradient outside the shock region is too small to have large effects on the line profiles and the shock itself occurs too high in the atmosphere to be of any
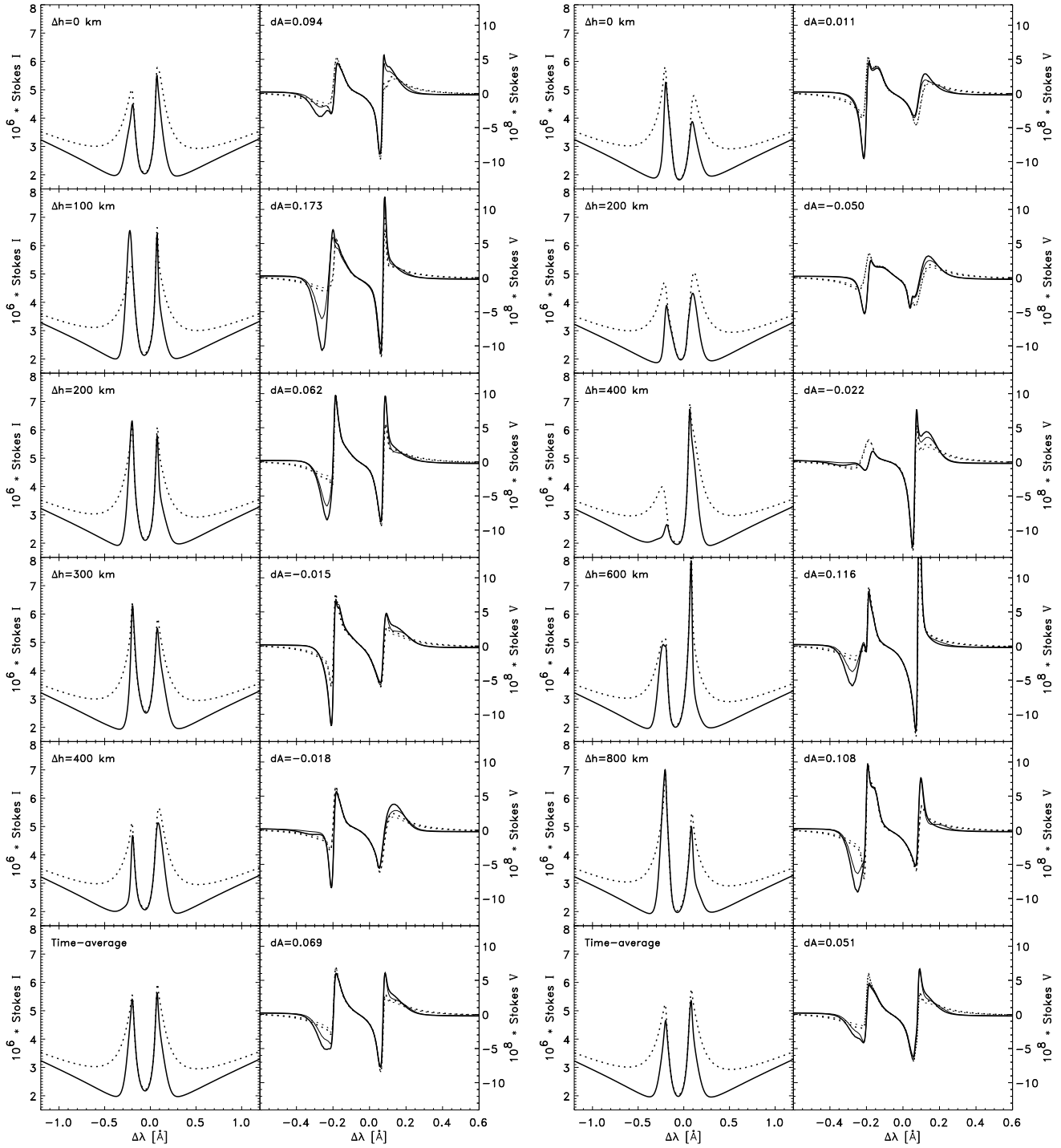
Fig. 18. Spatially-averaged Stokes I and V profiles for the FAL-F/FAL-C tube model with shocks (upflow) traveling upward inside the tube with a separation of 500 km (left half) and 1000 km (right half), respectively. The first 5 rows present the changes in the line profiles as the shock fronts move up in steps of 100 km, resp. 200 km. The last row shows the "time-average" of these profiles. Solid curves represent the PRD profiles and the dotted ones represent the CRD profiles. In the right column of each half the thick curves represent the computed Stokes V profiles and the thin curves represent the corresponding $-\mathrm{d}I/\mathrm{d}\lambda$. Note the factor of 2 difference between the I and V wavelength scales. dA values of the PRD V profiles are indicated
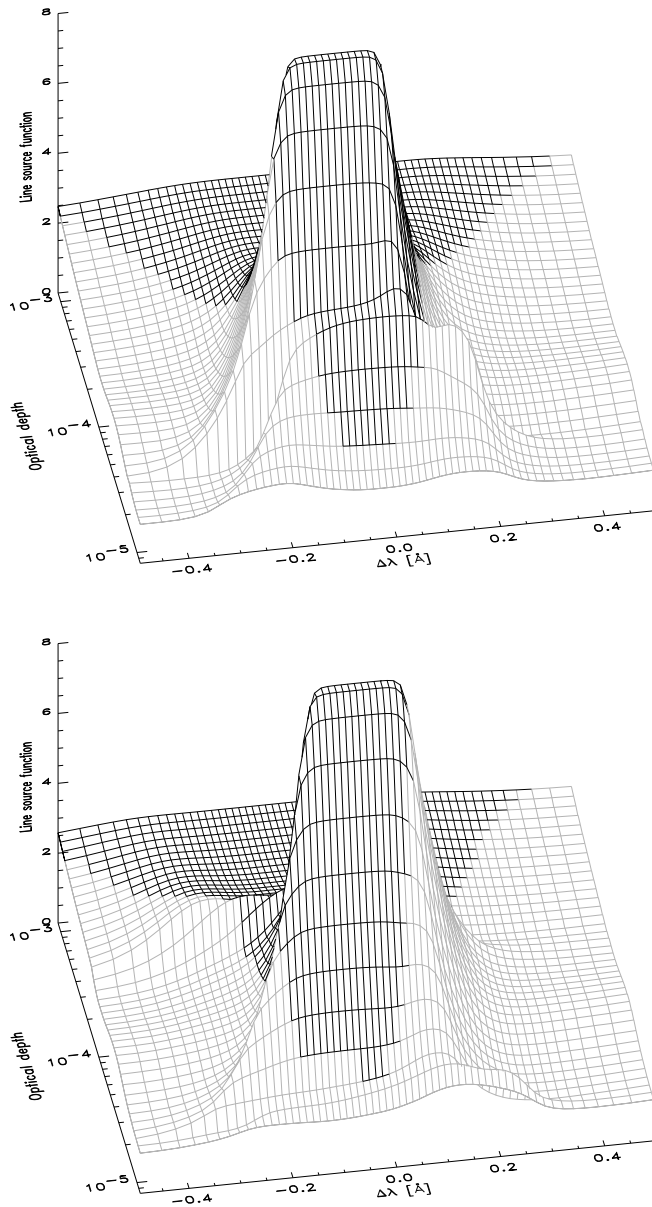
Fig. 19. PRD line source function vs. wavelength and standard continuum optical depth τ_5 for the central part of the Ca II K line in the upper part of ray 4 of the flux tube model with shocks inside the tube separated by 1000 km. This ray has been chosen far enough from tube center so that the line wings are formed in the non-magnetic part of the atmosphere, in order to suppress their Stokes V signature, but not so far that the line center part starts to sense the underlying non-magnetic region. The shocks in the model of the bottom panel are offset 400 km upward with respect to the shocks of the model in the top panel. The switch between the different shadings occurs at monochromatic optical depth unity

consequence beyond producing a small value for the Doppler shift of the line center. There is another shock deeper in the atmosphere, potentially relevant to the profile further out in the wing, but that has little impact since the wavelength dependence of the line source function is small there. The bottom panel of Fig. 19 shows the line source function for the same ray after the shocks have moved up by 400 km. The uppermost shock has now moved beyond the core formation region, but the next one is at a very crucial height, just at the onset of the chromospheric line source function bump. The shock shifts the line opacity in wavelength in such a way that over a certain range in wavelength just blueward of line center the atmosphere becomes optically thin within a very small height interval. This significantly reduces the strength of the K_{2V} peak, whereas K_{2R} gains strength. Such strong wavelength shifts are not very desirable from a computational point of view since they enhance the jumps in the optical depth grid and produce "noisy", slightly inaccurate line profiles. The influence is most visible in the Stokes V profiles.

7. Discussion

We have extended the Hubený & Lites (1995) angle-averaged PRD version of MULTI (Carlsson 1986) to include atmospheric models with velocity fields, which require the photon scattering matrix to be computed angle-dependently. Furthermore, we have extended the Murphy & Rees (1990) Stokes vector formal solution routine SPSR to take the wavelength dependence of the PRD line source function into account when solving for the Stokes vector.

The combination of these codes allows us to obtain the first computations of PRD Zeeman-split Stokes profiles, in particular of the Ca II K lines, which are expected to be more realistic than previous CRD profiles (Auer et al. 1977; Rees et al. 1989). Note that these are not the first PRD Stokes profiles, as, e.g., Faurobert-Scholl (1991, 1992, 1994) has computed PRD Stokes profiles of the Ca I 4227 Å resonance line. Those Stokes profiles, however, result from resonance polarization.

The angle-dependent PRD version of MULTI allows us to present the first PRD Stokes profiles in an atmosphere with flows. Thus, velocity gradients can be introduced and profile asymmetries can be analyzed. Milkey et al. (1975) also developed an angle-dependent PRD radiative transfer code, but their limited computer resources prohibited the use of a depth-dependent scattering matrix.

Finally, we present the first Ca II K Stokes profiles from flux tubes: another step towards the development of Ca II K into a diagnostic of the magnetic, thermal and dynamic structure of small-scale magnetic features.

Our main results can be summarized as follows:

– PRD Stokes Q, U, V profiles look more or less as expected from CRD computations. No really new features to the already complex CRD Stokes profiles appear, but the signal strength may change.
– The level of sophistication required for PRD Stokes profile computations depends on the Zeeman-splitting pattern of a line and on the magnetic field strength in the atmosphere.

In principle any splitting pattern and magnetic field strength can be handled, provided the correct PRD option is chosen in the SPSR code.

– For static flux tubes $V \sim \mathrm{d}I/\mathrm{d}\lambda$, but only when averaging over the whole flux tube. If the magnetic flux is not conserved with height in the resolution element, then this shows up clearly in departure of V from $\mathrm{d}I/\mathrm{d}\lambda$.

– Velocity gradients in and at the edge of the flux tube produce asymmetric V, whereby we must distinguish between an asymmetry between the blue and red K_2 peaks and between the positive and negative parts of V. Even in this case the weak-field approximation may provide a fairly accurate estimate of the spatially-averaged Stokes V profile. Only for the models with shocks do the differences between $\mathrm{d}I/\mathrm{d}\lambda$ and V become appreciable.

So far the only published observations of Ca II H & K Stokes (I and V) parameters are those of Martínez Pillet et al. (1990), del Toro Iniesta et al. (1991) and Trujillo-Bueno et al. (1993). They found an intriguing variety of line profile shapes, including highly asymmetric ones. Our calculations, in particular those including the effects of a velocity (gradient) also show a sizeable variety of profile shapes. Some of our profiles are similar to observed counterparts, others differ considerably. This may partly be due to insufficient statistics, too few observations and too few models considered here, or due to our limited selection of velocity stratifications. It may, however, also reflect our neglect of line broadening mechanisms such as macroturbulence.

It was not our aim to reproduce specific Ca II H & K observations, but rather to develop the tools needed to interpret such observations. Now that the diagnostic tools have been provided, it is time for new and systematic observations of Stokes profiles of the Ca II resonance lines.

References

Achmad L., de Jager C., Nieuwenhuijzen H., 1991, A&A 250, 445

Adams T. F., Hummer D. G., Rybicki G. B., 1971, J. Quant. Spectrosc. Radiat. Transfer 11, 1365

Auer L. H., Heasley J. N., House L. L., 1977, ApJ 216, 531

Auer L. H., Paletou F., 1994, A&A 284, 675

Avrett E. H., 1995, in J. R. Kuhn, M. J. Penn (eds.), Infrared tools for Solar Astrophysics: What's Next, Proc. 15th NSO/SP Summer Workshop, National Solar Observatory, Sunspot, p. 303

Bruls J. H. M. J., Trujillo Bueno J., 1996, Solar Phys. 164, 155

Bünte M., Solanki S. K., Steiner O., 1993, A&A 268, 736

Cannon C. J., Lopert P. B., Magnan C., 1975, A&A 42, 347

Cannon C. J., Vardavas I. M., 1974, A&A 32, 85

Carlsson M., 1986, A Computer Program for Solving Multi-Level Non-LTE Radiative Transfer Problems in Moving or Static Atmospheres, Report No. 33, Uppsala Astronomical Observatory

Carlsson M., Stein R. F., 1992, ApJ Let 397, 59

Carlsson M., Stein R. F., 1997, ApJ in press

del Toro Iniesta J. C., Martínez Pillet V., Vázquez M., 1991, in L. J. November (ed.), Solar Polarimetry, Proc. 11th NSO/SP Summer Workshop, National Solar Observatory, p. 224

Doschek G. A., Feldman U., Bohlin J. D., 1976, ApJ 205, L177

Farmer C. B., Norton R. H., 1989, A High-Resolution Atlas of the Infrared Spectrum of the Sun and the Earth Atmosphere from Space, NASA Ref. Publ. 1224, Vol. 1

Faurobert-Scholl M., 1991, A&A 246, 469

Faurobert-Scholl M., 1992, A&A 258, 521

Faurobert-Scholl M., 1994, A&A 285, 655

Feldman U., Cohen L., Doschek G. A., 1982, ApJ 255, 325

Fontenla J. M., Avrett E. H., Loeser R., 1991, ApJ 377, 712

Grossmann-Doerth U., Larsson B., Solanki S. K., 1988a, A&A 204, 266

Grossmann-Doerth U., Schüssler M., Solanki S. K., 1988b, A&A 206, L37

Heinzel P., 1981, J. Quant. Spectrosc. Radiat. Transfer 25, 483

Hubený I., 1981, Bull. Astron. Inst. Czech. 32, 271

Hubený I., 1982, J. Quant. Spectrosc. Radiat. Transfer 27, 593

Hubený I., 1985a, in J. E. Beckman, L. Crivellari (eds.), Progress in Stellar Spectral Line Formation Theory, NATO ASI Series C-152, Reidel, Dordrecht, p. 27

Hubený I., 1985b, Bull. Astron. Inst. Czech. 36, 1

Hubený I., Cooper J., 1986, ApJ 305, 852

Hubený I., Lites B. W., 1995, ApJ 455, 376

Hubený I., Oxenius J., Simonneau E., 1983a, J. Quant. Spectrosc. Radiat. Transfer 29, 477

Hubený I., Oxenius J., Simonneau E., 1983b, J. Quant. Spectrosc. Radiat. Transfer 29, 495

Hummer D. G., 1962, MNRAS 125, 21

Hummer D. G., 1968, MNRAS 141, 479

Hünerth G., Ulmschneider P., 1995, A&A 293, 166

Kunasz P. B., Auer L., 1988, J. Quant. Spectrosc. Radiat. Transfer 39, 67

Landi Degl'Innocenti E., 1985, Solar Phys. 102, 1

Landi Degl'Innocenti E., Landi Degl'Innocenti M., Landolfi M., 1997, in N. Mein (ed.), THEMIS Forum proceedings, in press

Linsky J. L., Avrett E. H., 1970, PASP 82, 169

Lites B. W., Bruner, Jr. E. C., Chipman E. G., Shine R. A., Rottman G. J., White O.R., Athay R. G., 1976, ApJ 210, L111

Magnan C., 1974, A&A 35, 233

Martínez Pillet V., García López R. J., del Toro Iniesta J. C., Rebolo R., Vázquez M., Beckman J. E., Char S., 1990, ApJ 361, L81

Martínez Pillet V., Lites B. W., Skumanich A., 1997, ApJ 474, 810

McKenna S. J., 1980, ApJ 242, 283

Mihalas D., 1978, Stellar Atmospheres, Freeman and Company, San Francisco, 2nd edition

Mihalas D., 1980a, ApJ 238, 1034

Mihalas D., 1980b, ApJ 238, 1042

Mihalas D., Shine R. A., Kunasz P. B., Hummer D. G., 1976, ApJ 205, 492

Milkey R. W., Shine R. A., Mihalas D., 1975, ApJ 202, 250

Murphy G. A., Rees D. E., 1990, Operation of the Stokes Profile Synthesis Routine, NCAR Technical Note NCAR/TN-348+IA, High Altitude Observatory, Boulder

Nagendra K. N., 1996, Solar Phys. 164, 67

Omont A., Smith E. W., Cooper J., 1972, ApJ 175, 185

Omont A., Smith E. W., Cooper J., 1973, ApJ 182, 283

Oxenius J., 1965, J. Quant. Spectrosc. Radiat. Transfer 5, 771

Paletou F., Auer L. H., 1995, A&A 297, 771

Rees D. E., 1969, Solar Phys. 10, 268

Rees D. E., Murphy G. A., Durrant C. J., 1989, ApJ 339, 1093

Rees D. E., Saliba G. J., 1982, A&A 115, 1

Reichel A., Vardavas I. M., 1975, J. Quant. Spectrosc. Radiat. Transfer 15, 929

Sanchez Almeida J., Collados M., del Toro Iniesta J. C., 1989, A&A 222, 311

Scharmer G. B., 1983, A&A 117, 83

Schrijver C. J., 1995, A&AR 6, 181

Solanki S. K., 1986, A&A 168, 311

Solanki S. K., 1989, A&A 224, 225

Solanki S. K., Bruls J. H. M. J., 1994, A&A 286, 269

Solanki S. K., Pahlke K. D., 1988, A&A 201, 143

Solanki S. K., Steiner O., 1990, A&A 234, 519

Solanki S. K., Steiner O., Uitenbroek H., 1991, A&A 250, 220

Stenflo J. O., Harvey J. W., 1985, Solar Phys. 95, 99

Streater A., Cooper J., Rees D. E., 1988, ApJ 335, 503

Trujillo-Bueno J., Martínez-Pillet V., Sánchez-Almeida J., Landi Degl'Innocenti E., 1993, in H. Zirin, G. Ai, H. Wang (eds.), The magnetic and velocity fields of solar active regions, Astronomical Soc. of the Pacific Conference Series, Vol. 46, p. 526

Uitenbroek H., 1989, A&A 213, 360

Ulmschneider P., 1994, A&A 288, 1021

Vardavas I. M., 1976, J. Quant. Spectrosc. Radiat. Transfer 16, 1

Vardavas I. M., Cannon C. J., 1976, A&A 53, 107